



저작자표시-비영리-변경금지 2.0 대한민국

이용자는 아래의 조건을 따르는 경우에 한하여 자유롭게

- 이 저작물을 복제, 배포, 전송, 전시, 공연 및 방송할 수 있습니다.

다음과 같은 조건을 따라야 합니다:



저작자표시. 귀하는 원저작자를 표시하여야 합니다.



비영리. 귀하는 이 저작물을 영리 목적으로 이용할 수 없습니다.



변경금지. 귀하는 이 저작물을 개작, 변형 또는 가공할 수 없습니다.

- 귀하는, 이 저작물의 재이용이나 배포의 경우, 이 저작물에 적용된 이용허락조건을 명확하게 나타내어야 합니다.
- 저작권자로부터 별도의 허가를 받으면 이러한 조건들은 적용되지 않습니다.

저작권법에 따른 이용자의 권리는 위의 내용에 의하여 영향을 받지 않습니다.

이것은 [이용허락규약\(Legal Code\)](#)을 이해하기 쉽게 요약한 것입니다.

[Disclaimer](#)

Master's Thesis

Versatile Scanning Optical Coherence Tomography
for Volumetric Multi-Scale Imaging

Hyeongeun Kim

Department of Biomedical Engineering

Graduate School of UNIST

2018

Versatile Scanning Optical Coherence Tomography for Volumetric Multi-Scale Imaging

Hyeongeun Kim

Department of Biomedical Engineering

Graduate School of UNIST

Versatile Scanning Optical Coherence Tomography for Volumetric Multi-Scale Imaging

A thesis/dissertation
submitted to the Graduate School of UNIST
in partial fulfillment of the
requirements for the degree of
Master of Science

Hyeongeun Kim

11. 23. 2017

Approved by



Advisor

Woonggyu Jung

Versatile Scanning Optical Coherence Tomography for Volumetric Multi-Scale Imaging

Hyeongeun Kim

This certifies that the thesis/dissertation of Hyeongeun Kim is approved.

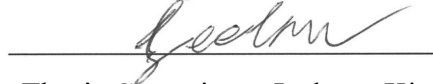
11/23/2017

signature



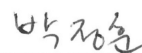
Advisor: Woonggyu Jung

signature



Thesis Committee: Jeehyun Kim

signature



Thesis Committee: Jung-Hoon Park

ABSTRACT

The optical imaging has a critical role in biomedical research to analyze functional and morphological variation of an organ, tissue and even a single cell of animal models. Since the optical imaging modality has features of indirect access, volumetric analysis and high resolution, it has been used for biomedical analysis. Especially, as a low coherence interferometric imaging technique, optical coherence tomography (OCT) has been applied in scientific and medical fields from few decades ago.

Since OCT can provide endogenous contrast of biological tissue using the infrared light source, it has high potential to be applied in practical medical diagnosis. However, it is hard to acquire uneven or thick sample due to the limited imaging window and penetration depth. To overcome those limitations, lots of optical, mathematical and chemical solutions comes within a decade such as adaptive optics, full-range method and tissue clearing. Despite the existence of suggested solutions, practical application of OCT is limitation due to the cost of time and effort.

Here, we present practical methods to enhance acquirable endogenous information of sample through versatile scanning optical coherence tomography(VS-OCT). Conventional OCT utilizes dual-axis based flat focal plane scanning method providing limited depth information of curved samples. Thus, we developed advanced OCT, called VS-OCT, which can fully optimize imaging window by changing focal plane to dual plane and cylindrical plane. The VS-OCT is demonstrated for 1) quantification of engineered skin, 2) monitoring of tadpole development, 3) screening phenotype of zebrafish and 4) quantification of spinal cord injury (SCI) of mouse.

Key words: Optical Coherence Tomography (OCT), Versatile Scanning Optical Coherence Tomography (VS-OCT), Optical Imaging, Imaging Depth

CONTENTS

1. Introduction	1
1.1. Motivation for Research.....	2
1.2. Current Techniques for Deep Tissue Imaging.....	3
1.3. Overview: Versatile Scanning Optical Coherence Tomography.....	4
2. Theory of Optical Coherence Tomography	5
2.1. Image Resolution.....	5
2.2. Interferometry.....	6
2.2.1. Michaelson Interferometer	6
2.2.2. Mach-Zehnder Interferometer	7
2.3. Image Acquisition	8
2.4. Spectral Domain Optical Coherence Tomography.....	9
2.4.1. SD-OCT Hardware & Software.....	13
2.5. Swept Source Optical Coherence Tomography.....	16
2.5.1. SS-OCT Hardware & Software	18
3. System Development	21
3.1. Co-axial Vertical Scanning OCT.....	21
3.1.1. Hardware Setup	21
3.1.2. Image Calibration	23
3.2. Circular scanning OCT.....	25
3.2.1. Hardware Setup	25
3.2.2. Image Reconstruction	27
4. Application.....	29
4.1. Quantification of Engineered Skin.....	29
4.2. Monitoring of Tadpole Development.....	31
4.3. Monitoring of Zebrafish Development	33
4.4. Quantification of Spinal Cord Injury	35
5. Discussion and Conclusion	40

LIST OF FIGURES

Figure 1.1 Comparison of imaging modalities in terms of resolution and penetration depth ..	1
Figure 1.2 Schematic diagram for versatile scanning OCT.....	4
Figure 2.1 Specification of Gaussian spectrum laser source(left) and lens(right).....	5
Figure 2.2 Schematics for Michaelson interferometry for spectral domain OCT	6
Figure 2.3 Mach-Zehnder Interferometry in air and optical fiber	7
Figure 2.4 Terminology and meaning for scanning mode of OCT.....	8
Figure 2.5 Signal profiles of SD-OCT system.....	10
Figure 2.6 Conventional spectrometer without k-linearlization	11
Figure 2.7 k-linearlized spectrometer with prism.....	11
Figure 2.8 Setup for transmission type grating based spectrometer.....	12
Figure 2.9 Hardware setup for SD-OCT	13
Figure 2.10 Operation algorithm for spectral domain OCT	15
Figure 2.11 Signal profile and FFT of Hann windowed signa	17
Figure 2.12 Hardware setup for SS-OCT	18
Figure 2.13 Operation algorithm for swept source OCT.....	20
Figure 3.1 System schematics for co-axial vertical scanning OCT.....	22
Figure 3.2 Hand-held type scanner of co-axial vertical scanning probe	22
Figure 3.3 Calibration film for co-axial vertical scanning OCT	24
Figure 3.4 Algorithm for mapping top and bottom images	24
Figure 3.5 Schematic diagram for circular scanning OCT and real.	26
Figure 3.6 Comparison of conventional and linear scanning system	26
Figure 3.7 3D reconstructed image of pen through circular scanning OCT.....	27
Figure 3.8 Coordination conversion for circular scanning OCT	28
Figure 4.1 3D reconstructed image and cross-section image of engineered skin.....	30
Figure 4.2 Merged image of top and bottom and segmentation of wound region.....	30
Figure 4.3 Tomographic image of tadpole embryo and A-line profile at different stage.....	31

Figure 4.4 Volumetric analysis of <i>Xenopus laevis</i>	32
Figure 4.5 Visualization of Zebrafish and its heart at 48pfh	33
Figure 4.6 Developmental monitoring of Zebrafish using various imaging techniques	34
Figure 4.7 Histology of mouse spinal cord stained with H&E and LFB.....	36
Figure 4.8 Cross-sectional demonstration of mouse spinal cord using OCM	36
Figure 4.9 Image segmentation of spinal cord injury of mouse	38
Figure 4.10 Sample preparation of spinal cord and 3D reconstructed image.....	39
Figure 5.1 Visualization of vascular deformation using OCT and fluorescence microscope.	40
Figure 5.2 Simulation of full-range application with additional phase modulation	42
Figure 5.3 Flow-chart and code for full-range algorithm.....	42

1. Introduction

Optical imaging apparatus has a critical role in biomedical study to analyze functional and morphological variation of organ, tissue and even single cell level [1-4]. In comparison with other imaging modalities such as MRI and X-rays, optical approaches offer high sensitivity and better endogenous or exogenous contrast with high spatial resolution as shown in **Figure1.1**. Also by utilizing fluorescence tagging method, it is possible to selectively visualize targeted cell through fluorescence microscopy [5-6]. The advanced optical and mechanical technique allows not only tomographic image but also volumetric analysis with several micrometer resolution in real-time [7-9]. One of the possible methods is optical coherence tomography (OCT) which is an optical imaging technique based on low coherence interferometer [4, 10]. OCT non-invasively provide tomographic image of high resolution. visualize sample without any fluorescence tag and depth-resolved information with sub-micrometer resolution without physical damage. However, OCT still has a limitation in terms of imaging depth due to the given imaging window size. Although several chemical, optical and mathematical methods have been provided, it is hard to apply in practical.

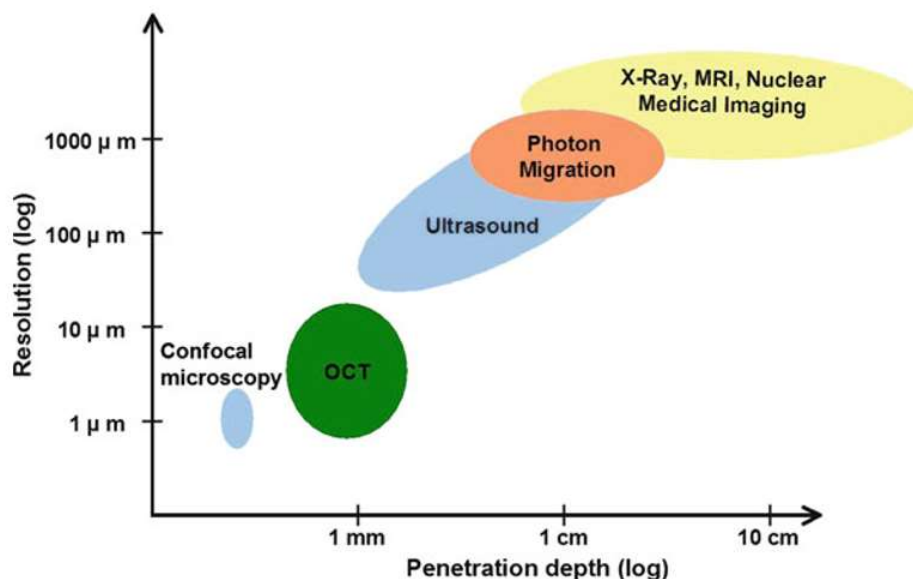


Figure 1.1 Comparison of imaging modalities in terms of resolution and penetration depth

1.1. Motivation for Research

Recently, OCT was applied to medical field for cancer detection, skin diagnosis and ophthalmological analysis [11-14]. For several analyses of sectioned sample, OCT with high NA objective lens, called optical coherence microscopy (OCM) has been applied to visualize micro structure without chemical staining [15-16]. Many high-resolution microscopy techniques work well on thin and nearly transparent samples, but in most realistic scenarios it is required to obtain information at depth within *in vivo* tissue. Unfortunately, biological tissues are heterogeneous at all length scales: the resulting heterogeneities of the refractive index affect light propagation through tissue, and induce perturbations of the light wavefront, conventionally described as aberrations and scattering [17].

In terms of the physical characteristics of light, the trade-off relationship between imaging resolution and depth is it is definite. During the large scale volumetric imaging, the given value of imaging condition could limit imaging quality or imaging depth. To acquire deep tissue tomographic images preserving high-resolution endogenous contrast, several techniques have been developed through chemical, mechanical and optical ways [18-25]. However, those solution requires equivalent temporal or computational cost and additional optical components. Thus, we focused on the method that can improve imaging depth limitation without additional procedure.

The conventional OCT acquire tomographic image within given imaging window using reflective linear scanning mirror. Since the scan motion is linear, the focusing position after objective lens is flat line or flat plane for 3-dimensional scanning. Meanwhile, for a sample of large thickness or high curvature, the linear scanning method cannot fully visualize internal structure. The main important points for deep tissue imaging are not only enhancement of the imaging depth but also full utilization of imaging window. Therefore, the versatile scanning optical coherence tomography method could provide optimal scanning method according to the shape of sample and fully utilize imaging window.

1.2. Current Techniques for Deep Tissue Imaging

As a traditional imaging methodology, light microscopy has been a gold standard for visualizing detail structure of tissue through histology [26]. After the invention of fluorescence microscopy and confocal microscopy, it has been possible to visualize more detailed information of cell level selectively [5-6]. However, high-resolution characteristic cannot solve the enhancement of imaging depth simultaneously, resulting several hundreds of micrometers.

Since a decade ago, the tissue clearing method has been introduced for optical imaging modality as a breakthrough technique to increase the possible imaging window by making sample transparent [18, 27-28]. The suggested method can be applied in optical projection tomography (OPT) for neuronal and embryonic study [29-31]. For the OCT, although the solution can help enhancement of imaging depth, the contrast also might be affected by chemical solution. In addition, it requires multiple procedure and bio-toxic agent, limiting its application for *ex-vivo* study.

Meanwhile, the optical and mathematical advances on OCT have brought enhancement of imaging depth. The limitation of imaging depth originates from heterogeneities of the refractive index which affect light propagation through tissue. With the digital micromirror device(DMD), the distorted wavefront propagation can be compensated through complex wavefront-shaping method [25, 27]. However, it requires complicate computational cost to calculating wavefront reversely. The well-known method for deep tissue imaging is application of long wavelength laser source for optical imaging. As optical techniques have been advanced, 1.7 μ m center wavelength laser source was developed, providing small enhancement at penetration depth [23].

Another mechanical method for depth increment is physical change of scan motion. The dual-scanning OCT and rotational scanning OCT were proposed by merging multi-side images to single image. It could reduce the temporal cost for sample preparation, however, the additional dual axis scanner and rotational stage is required to visualize 3-dimensional structure of merged image. Although several studies already combined above solutions with OCT to acquire deep endogenous structure [27], our study focused on a practical solution which can be applied to other laser scanning imaging apparatus.

1.3. Overview: Versatile Scanning Optical Coherence Tomography

Since the OCT has its inborn limitation in terms of imaging depth, we propose a practical method to enhance imaging depth and provide volumetric images through versatile scanning OCT (VS-OCT) system.

The conventional OCT generates 3-dimensional image with A-mode scan of depth direction, B-mode scan of horizontal direction and C-mode scan of volumetric direction. Those three type of scanning method result the single flat imaging plane generating rectangular imaging window. It is true that OCT can help to visualize successful tomographic images for a sample of flat shape. However, conventional scanning method cannot interpret entire depth information of sample of high curvature or large thickness due to its limited penetration depth and imaging window as shown in Figure 1.2 (a). Thus, we applied versatile scanning method appropriate to the shape of sample. Especially for this study, we developed two types of scanner, co-axial vertical scanner with dual flat imaging plane (b) and circular scanner with cylindrical imaging plane (c), respectively.

The co-axial vertical scanner was demonstrated for quantifying the defect of engineered skin, visualizing internal organs of *Xenopus Larvae* tadpole, and monitoring the phenotype expression onto *Zebrafish*. Meanwhile, the circular scanner was applied to analyze volumetric size of spinal cord injury (SCI).

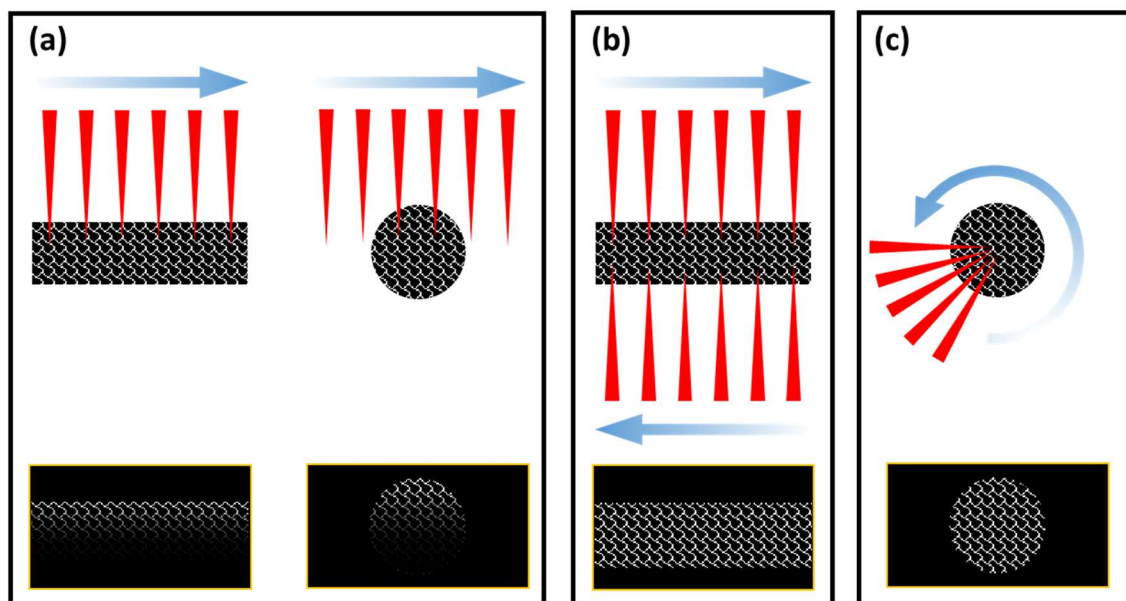


Figure 1.2 Schematic diagram for versatile scanning OCT

2. Theory of Optical Coherence Tomography

OCT applies low-coherence interferometry to produce a 2-dimensional tomographic image of a sample in the way that is analogous to ultrasound imaging. The most important part of OCT is physical characteristics of laser source and type of interferometer. Detailed explanations will be followed.

2.1. Image Resolution

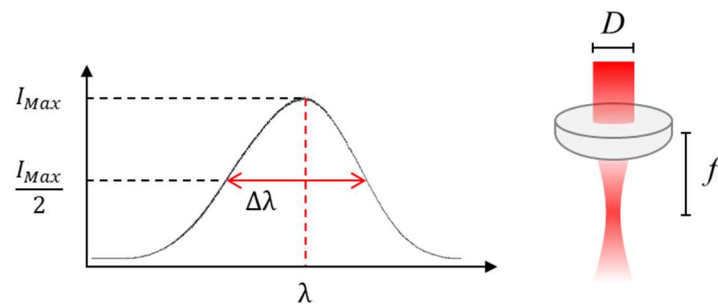


Figure 2.1 Specification of Gaussian spectrum laser source(left) and lens(right)

Different from the conventional optical imaging system, OCT can provide tomographic image and thus, it has independent axial and lateral resolutions. The axial resolution is governed by the coherence length of light source and the lateral resolution is determined by the beam-focusing conditions. Especially for a laser source with a Gaussian wavelength spectrum, the axial and lateral resolutions are separately defined as

$$\Delta z = \frac{2 \ln 2}{\pi} \left(\frac{\lambda^2}{\Delta \lambda} \right)$$

$$\Delta x = \frac{4 \lambda}{\pi} \left(\frac{f}{d} \right)$$

where λ represents the center wavelength of laser source, $\Delta \lambda$ is the FWHM of laser source spectrum, d is the collimated beam diameter on the objective lens, and f is focal length of the objective lens, respectively.

2.2. Interferometry

For frequency domain OCT, the depth information is encoded as frequency of fringe signal generated by interference of two independent light pathways of sample and reference. If two different optical paths have optical delay within a coherence length, they are in coherent generating special fringe patterns according to the superposition theory of waves. For frequency domain OCT system, mainly two types of interferometer are commonly used.

2.2.1. Michaelson Interferometer

The Michaelson Interferometer was invented by Albert Abraham Michelson. He simply put a beam splitter after collimated light source, dividing incident laser into the different orthogonal pathways. Each of two beams propagates at a given optical pathlength, and hit target and mirror respectively. The back reflected light, or back scattered light, from each pathway starts to be combined at the beam splitter, generating optical fringe patterns. For the fiber based OCT system, instead of beam splitter, a fiber coupler can divide and converge optical signals. In frequency domain OCT, the axial depth information is encoded in fringe pattern as a relationship of depth and frequency. The upper part of sample is represented as low frequency, and lower part of sample is represented as high frequency. Since the final terminal of Michaelson interferometer has single output for detection, it has been selected as a standard interferometer for spectral domain OCT.

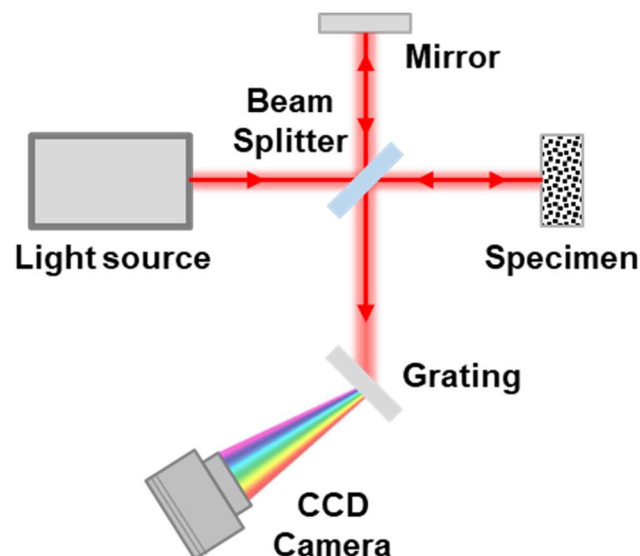


Figure 2.2 Schematics for Michaelson interferometry for spectral domain OCT

2.2.2. Mach-Zehnder Interferometer

The Mach-Zehnder interferometer is a device to figure out the relative phase variation between two optical beams separated from single light source. The apparatus is named with two physicists, Ludwig Mach and Ludwig Zehnder after its invention. The principle of Mach-Zehnder is similar with that of Michaelson, except it utilizes two beam splitters for single directional propagation of light. When this system is converted as fiber optics, additional optical components called circulator, which isolate outgoing beam path from incident beam. Since Mach-Zehnder interferometer gives two terminals as positive and negative for detection, it gives better signal-to-noise ratio comparing to the Michaelson interferometer [32].

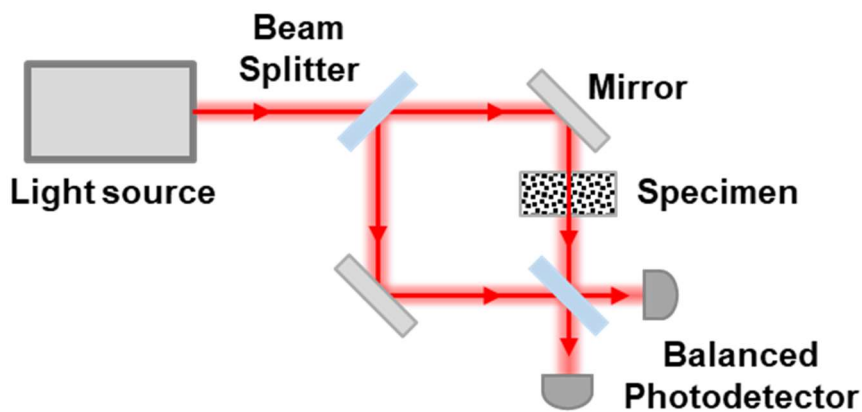


Figure 2.3 Mach-Zehnder Interferometry in air and optical fiber

2.3. Image Acquisition

After the light propagates and converges within a beam splitter or fiber coupler, the detector such as camera or balanced photodetector can visualize a depth information of a single focused beam position, called A-scan. To generate 2-dimensional cross-section image, the focused laser beam on a sample should be transposed across a horizontal direction of where we want to visualize. Using a rotational actuator with small mirror, the laser can scan lateral direction as B-scan, providing tomographic image of sample. After acquiring single B-scan image, another rotational actuator can move laser toward the orthogonal direction of image, called C-scan. The multiple tomographic images are stacked as virtual sectioned images and finally reconstructed as endogenous 3-dimensional object. Since the scanner helps laser to move on lateral direction, imaging plane has flat, horizontal shape.

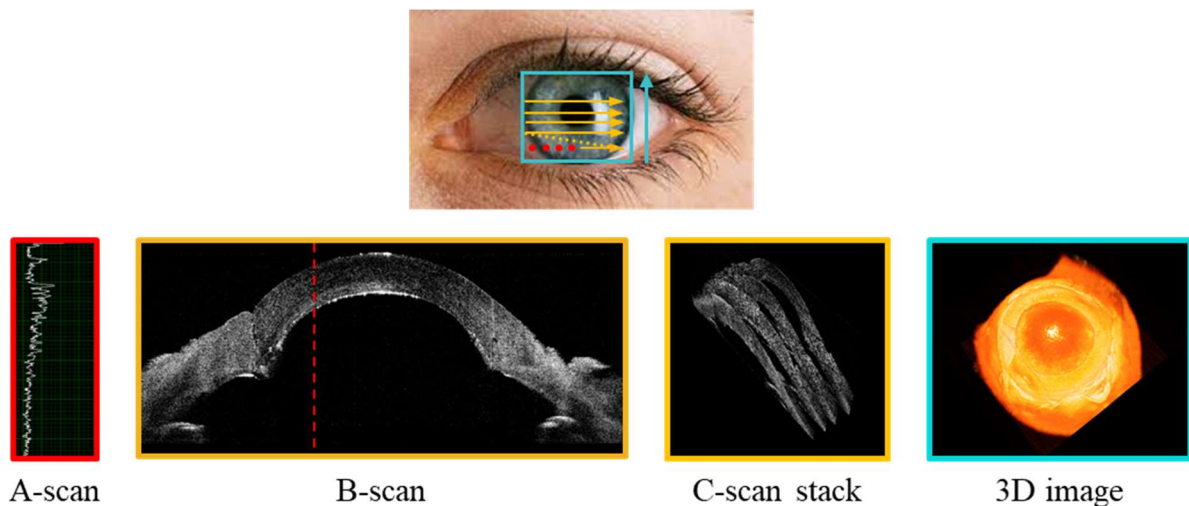


Figure 2.4 Terminology and meaning for scanning mode of OCT

For detection of optical fringe signal, two different types of hardware setup exist. Using the line scan camera and grating lens, the optical signal become spatially separated generating spectrum across pixels of camera in spectral domain OCT (SD-OCT). The other type of detector hardware is balanced photodetector with high speed digitizer. The apparatus is normally for swept source OCT (SS-OCT) system. Thus, according to the detector type, the frequency domain OCT system can be separated as SD-OCT and SS-OCT.

2.4. Spectral Domain Optical Coherence Tomography

The spectral domain optical coherence tomography (SD-OCT) detects signal based on the spectrometer with line CCD camera. The spectrometer is composed of collimator, reflective grating, focusing lens and line CCD camera to analyze spectrum changes. For SD-OCT, laser source has wavelength spectrum of Gaussian shape with given FWHM bandwidth.

The fringe patterns come out with a shape of Gaussian, which results low frequency DC noise after Fourier transform. Also, the camera pixel and wavelength of spectrum has non-linear relationship, resulting distortion of depth signal profile. To solve those problem, we applied several correction methods through software.

- **Background subtraction**

The fringe signals are added up to the envelope of Gaussian signal which comes from original spectrum shape of source. If the Fourier transform applies to the raw signal profile as shown in top of Figure 2.5, there exist strong DC noise on the top of the cross-section image. To reduce the DC noise intensity, we block optical path of sample arm to acquire only signal from reference. Since most of Gaussian spectrum comes from reference to generate optical fringe, only reference signal is recorded as background signal. After recording the reference signal, open the optical path of sample and acquire raw profile of fringe. Now, there exist two options, subtract background noise before Fourier transform (black line); and after Fourier transform (red line). The first method shows 44.7dB for noise, 71.3dB for signal intensity and second method gives 2.39dB for noise, 29.1dB for signal intensity. The SNR of those two methods are 26.6dB and 26.7dB which has no significant difference. Although there exists no big difference between two methods in terms of SNR, computational cost for second method is relatively high since it requires additional Fourier transformation of background noise. If we can save the Fourier transformed data of background signal, truly those two methods would give similar quality of tomographic image.

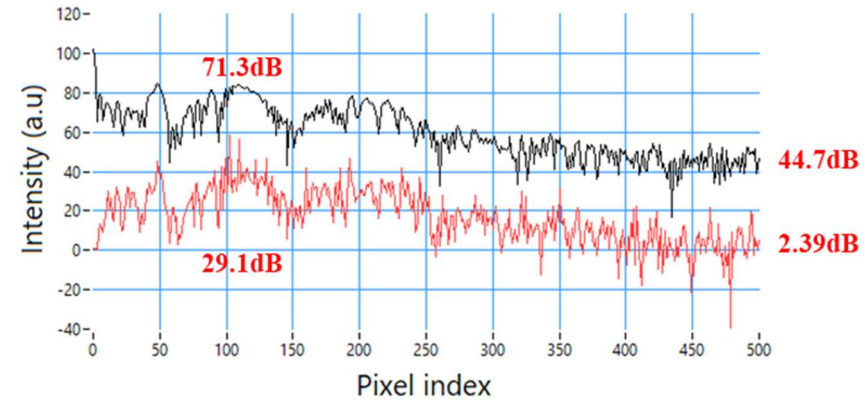
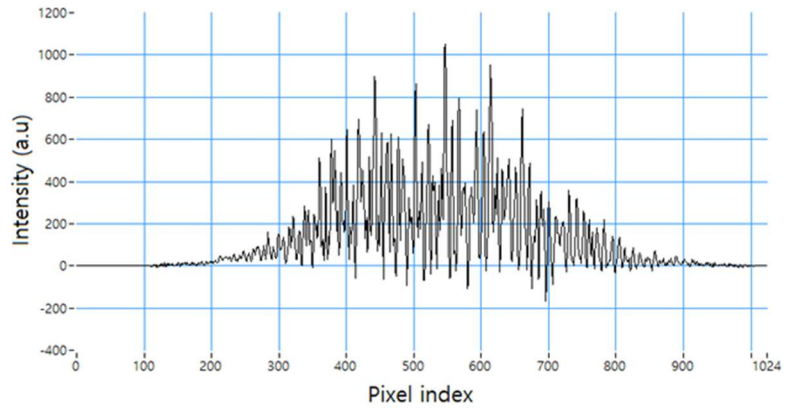
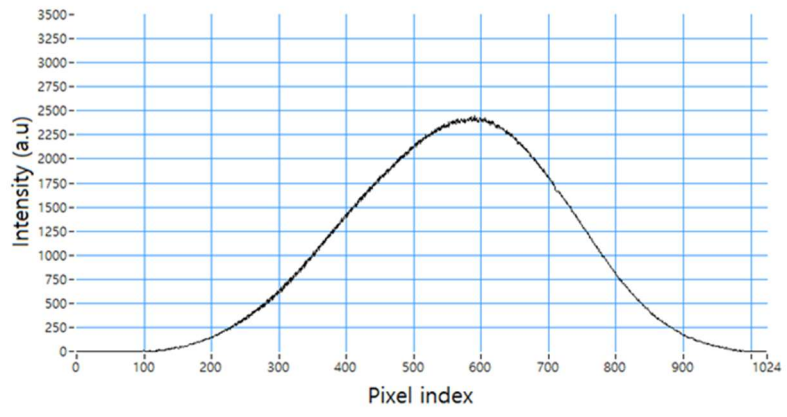
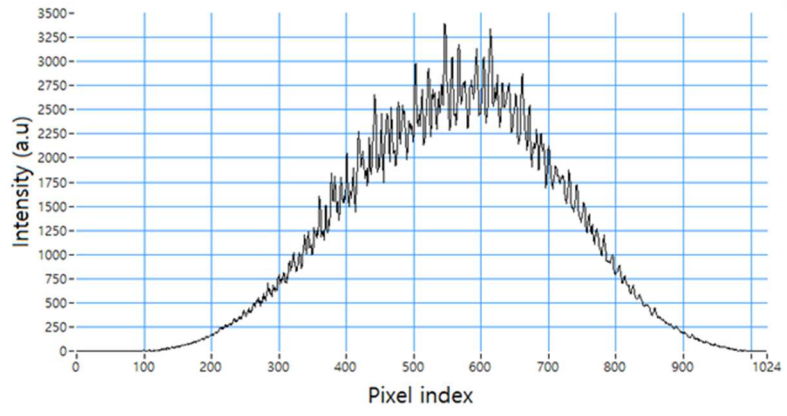


Figure 2.5 Signal profiles of SD-OCT system.

- **Spectrum k-linearization**

For the SD-OCT, the spectrometer design plays an important role in terms of specification of imaging system. The grating lens reflects collimation beam with different angle of different wavelength, generating spectral distribution across position. After the dispersed beam pass through objective lens, each wavelength lights are focused onto each pixel with a given bandwidth of spectrum. However, it has non-linear relationship between camera pixel and wavelength, or wavenumber (k) of focused light as shown in **Figure 2.6**.

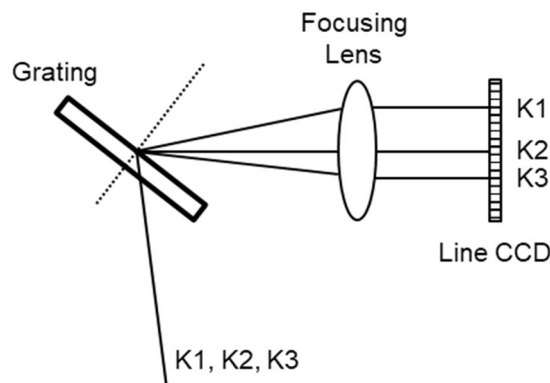


Figure 2.6 Conventional spectrometer without k-linearization

The non-linear relationship between pixel and wavenumber could cause distortion of image since final tomographic image is generated through Fourier transformation which deals with physical pixels on CCD camera. Without the compensation of non-linear relationship, we could acquire shallow depth information with broaden peaks.

There exist two ways to solve the non-linear relationship between pixel and wavenumber. First solution is insertion of prism at the middle of grating lens and objective lens as shown in **Figure 2.7** [33]. Since grating generates non-linearity, another non-linear characteristic component could waive the phenomenon. The prism can work as invert non-linear components resulting linear spectrum.

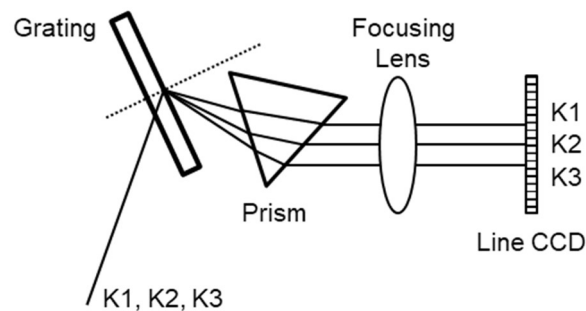


Figure 2.7 k-linearized spectrometer with prism.

However, as it needs additional optical component and requires finite optical alignment, we tried another method based on the software calibration without extra components [34]. If we can figure out which wavelength is focused on which pixel, then we could re-arrange acquired light spectrum by shifting several pixels.

The optimal k-linearization method depends on its application. If the OCT system requires fast imaging speed, the prism based k-linearization method is preferred due to the time cost for index re-mapping procedure is not required. For our application, software based k-linearization gives enough imaging speed, only taking few milliseconds to re-arrange single 2-dimensional cross-section image. Therefore, we designed spectrometer for center wavelength of 845nm and 20nm bandwidth laser source in **Figure 2.8**.

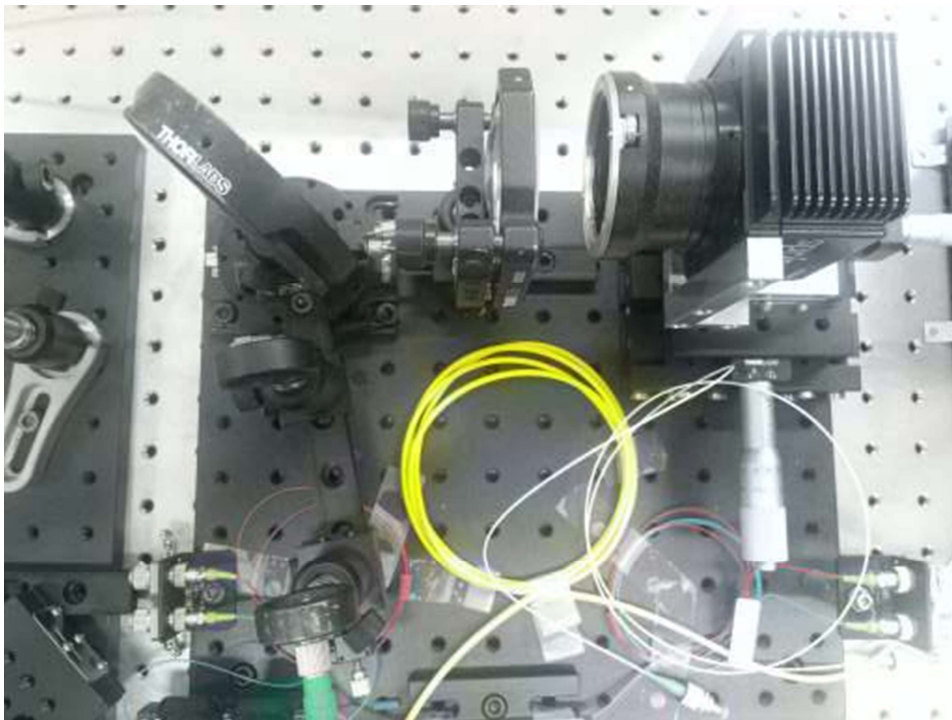


Figure 2.8 Setup for transmission type grating based spectrometer

2.4.1. SD-OCT Hardware & Software

- **Hardware setup**

For SD-OCT system, we used laser source with center wavelength of 845nm, and bandwidth of 50nm. The emitted laser is divided into two independent pathways through 50:50 fiber coupler (Thorlabs, TW805R5A2) to compose Michaelson interferometer. Since a lateral resolution has inverse proportional relationship with the beam diameter, we applied collimator (Thorlabs, F810APC-842) that can generate large diameter of collimated beam to the dual axis galvanomirror. The actuation of dual axis galvanomirror is controlled by data acquisition (DAQ) board through variable analog voltage signal. The galvanomirror is non-resonance type, which means it moves a specific angle according to a given voltage. To remove the dispersion and match the optical path length of sample and reference arm, the dispersion compensator (Thorlabs, LSM03DC) is inserted into the reference arm.

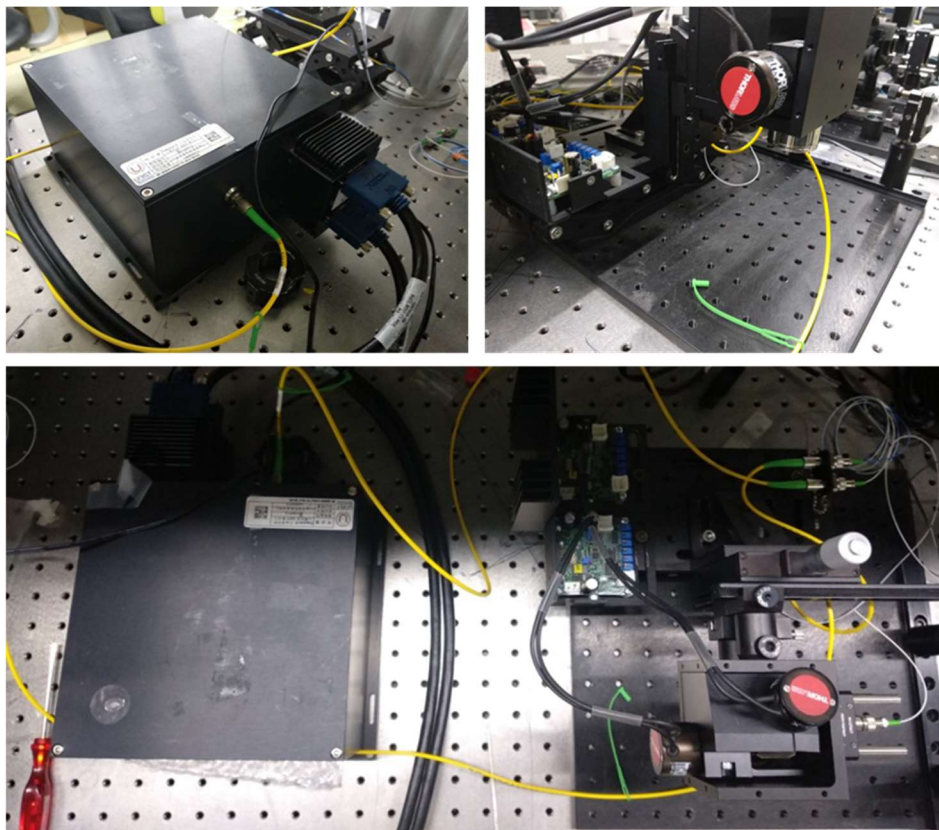


Figure 2.9 Hardware setup for SD-OCT

- **Control software**

To control the SD-OCT system, LabVIEW was used by acquiring camera data and actuating galvanomirror together. For SD-OCT, single A-line profile is generated through single shot of line scan camera (Basler, Spl-2048-140k) and frame grabber (NI, PCI-e 1447). To scan the laser with two independent axis galvanomirror (Thorlabs, GVS012), the data acquisition (DAQ) board (NI, PCI-e 1433) was used. The camera has maximum 140kHz acquisition speed, which means 140,000 A-lines/s sampling speed. If 500 of A-lines provide single B-mode image, it could visualize tomographic image with a speed of 280 frame/s. However, there exist two possible bottle-neck due to the throughput of PCI-e communication of grabber and signal processing time of central processing unit (CPU) or graphic processing unit (GPU). To construct a high-speed imaging system, GPU (Nvidia, GTX970) and CUDA software (Nvidia, v6.5) was applied. The most important part of SD-OCT software is synchronization of camera, galvanomirror and DAQ. As shown in Figure 3.2 with red color, single master trigger from DAQ controls camera and galvanomirror together. By setting the camera as an external trigger mode, it catches single A-line profile at single pulse of trigger signal. At the same time, the master clock signal is utilized as a clock source of analog output from DAQ, which actuate galvanomirror to tilt small unit angle at each A-line acquisition. To acquire a B-mode image, a given number of A-line profiles should be accumulated on the memory and transferred to the GPU for the Fourier transform of raw profile.

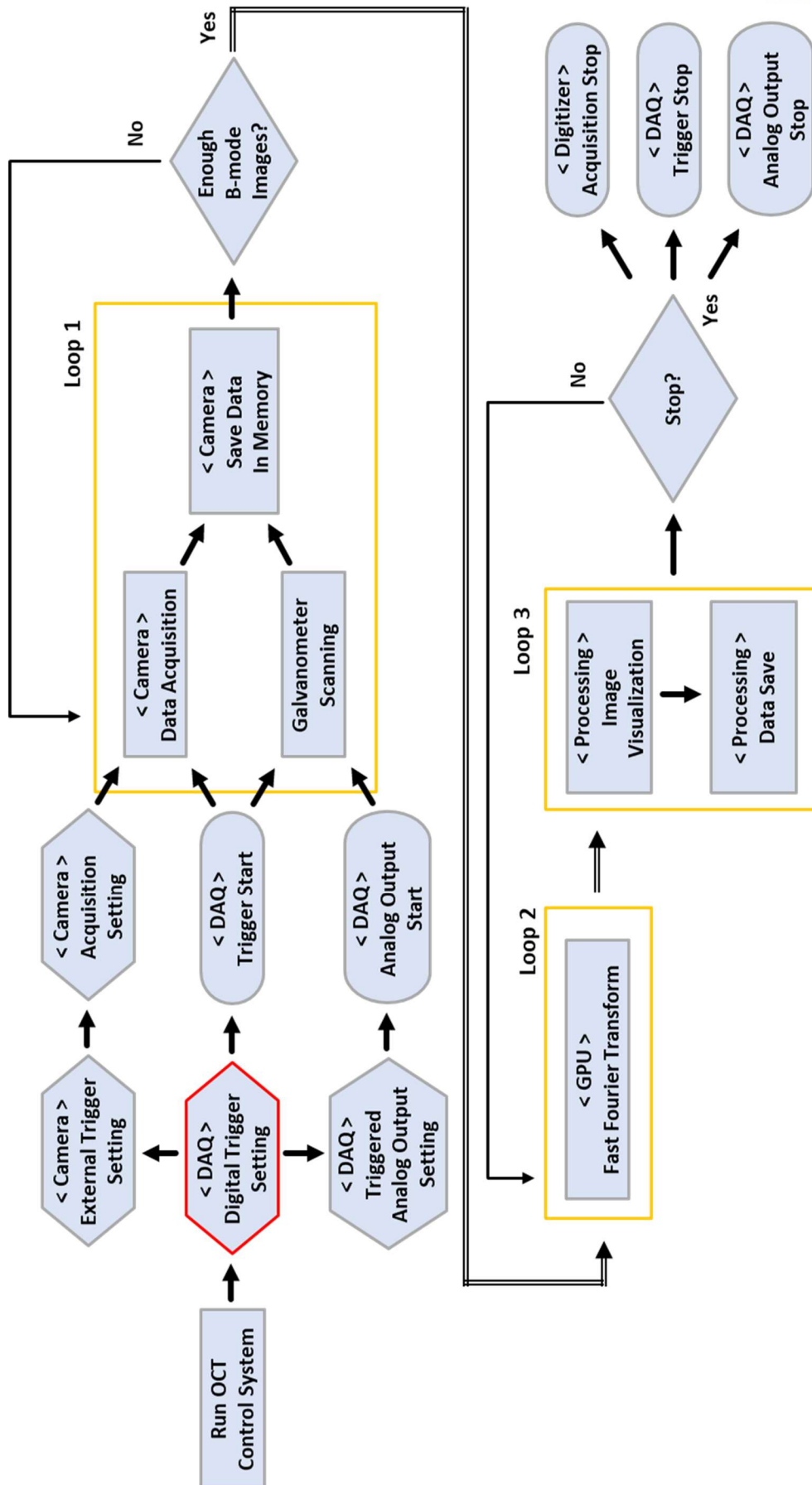


Figure 2.10 Operation algorithm for spectral domain OCT

2.5. Swept Source Optical Coherence Tomography

As a frequency domain OCT, the swept source OCT (SS-OCT) utilizes special type of laser source called sweep laser. Different from the normal laser source of SD-OCT which emits broadband spectrum at once, the sweep laser emits discrete narrow spectrum according to a time. When the laser turned on, it starts to sweep wavelength of light within a given bandwidth. For a depth encoded optical signal, Mach-Zehnder interferometer is applied with balanced photodetector and digitizer. The SS-OCT requires additional pre-signal processing before the Fourier transformation.

- **Signal windowing**

The acquired A-line profile has no DC offset nor gaussian shape due to the balanced photodetector, expecting better quality after Fourier transform. However, the result shows broaden profile as represented in last black plot of Figure 2.8. Since the truncated raw signal profile at both end gives high dysconnectivity, it is essential to set zero-padding of each end of signal. By applying zero paddings at both end of signal, discrete Fourier transform could recognize it as a continuous signal. However, just adding zeros is not enough to solve disconnection of signal. For that reason, we applied Hann windowing method to make zero-end signal without signal distortion. The Hann profile is given with following equation, similar with gaussian signal form.

$$w[n] = \frac{1}{2} \left(1 - \cos \left(\frac{2\pi n}{N-1} \right) \right)$$

Through Hann windowing, the Fourier transformed signal can be represented as $S(k)$ in Equation 2.4 and gives sharp and better signal-to-noise ratio (SNR) as shown in red plot of Figure 2.8.

$$S[k] = \sum_{n=0}^{N-1} s[n] \cdot w[n] \cdot e^{-j2\pi nk/N}$$

Since all the signals are acquired through digitizer based on k-clock of sweep laser source, no additional k-linearization process is required.

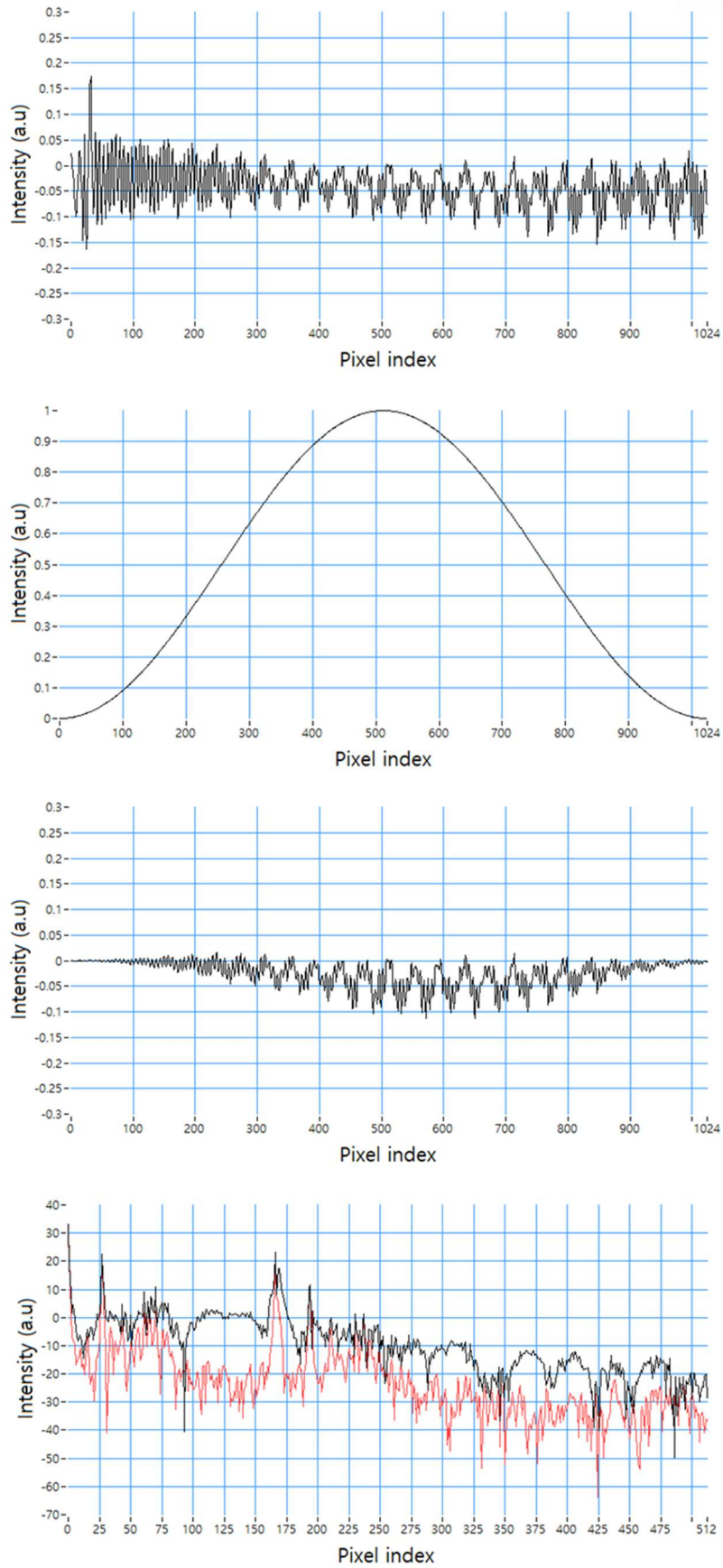


Figure 2.11 Signal profile and FFT of Hann windowed signal

2.5.1. SS-OCT Hardware & Software

- **Hardware setup**

The swept source OCT operates tomographic imaging of sample with sweep laser source (Axsun, 1310nm). The given k-clock speed of source is 100kHz, which means it could generate 100,000 A-lines per a second and 100 frames per second if single B-mode image is constructed with 1,000 A-lines. However, the possible bottle neck of those fast imaging OCT is acquisition speed of digitizer, data transfer bandwidth of bus, and computational cost for Fourier transform. Since the digitizer (Alazartech, ATS9350) used in our SS-OCT has ability to acquire $500 \cdot 10^6$ samples per second, the digitizer has enough speed for acquiring 1088 sample points per single A-line signal. The actual bottle neck is computational cost for Fourier transform of raw data. Every single 2-dimensional tomographic image contains $1088 \cdot 1000 \cdot 2$ bytes of data size and it takes ~ 11 ms per second through GPU (Nvidia, GTX970), which results lagging of data. Not only for the GPU, the scanning speed of galvanomirror (Thorlabs, GVS012) also could block maximum speed. Thus, we applied triangular scan to acquire OCT image without any rest of time. The other optical components are same with those of SD-OCT system. The final imaging speed of SS-OCT system is 100 frame/s with a condition of 1088 sample/A-line, 500 A-line/B-mode. If we decrease the sampling number for each A-line and B-mode, it is possible to visualize real-time 3D OCT image.

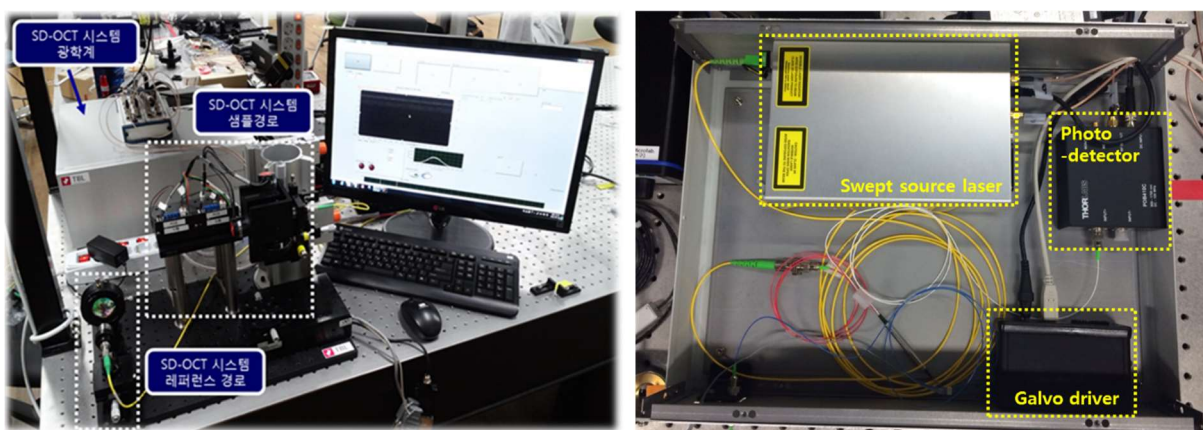


Figure 2.12 Hardware setup for SS-OCT

- **Control software**

The master clock signal is provided by Mach-Zehnder interferometer (MZI) inside of the sweep laser source which is different from SD-OCT. The MZI generates k-clock signal based on its wavenumber so that each signal acquisition point is matched with each wavelength. Therefore, SS-OCT requires no k-linearization if the trigger is synchronized correctly. Another digital from the laser source is A-mode trigger, which ensure the starting and ending of single sweep of wavelength. Using those two digital signals from the source, we could synchronize acquisition of photodetector signal and actuation of galvanomirror without hardware delay. The master k-clock from source is connected to the external clock port of digitizer to acquire wavelength matched signal. Then the A-trigger signal from the source is connected to the external trigger port of digitizer to trigger signal acquisition at the starting of laser sweeping. The A-trigger also can be used as a clock signal for galvanomirror movement since galvanomirror moves single point right after it acquires single A-line. After completing all hardware connection between each component, the software starts to process raw signal into tomographic image with a given setting value of digitizer.

Similar with the camera setting at SD-OCT system, the digitizer also has initial setting for signal recording length of B-mode. If the B-mode image is composed of 1000 A-line profiles with 1088 sampling number, then 1088,000 points of data is saved in the digitizer onboard memory. After finishing the acquisition, the cluster of data is transferred to the computer memory and starts to Fourier transform through CUDA parallel processing (Nvidia, v6.5). The background subtraction and data save procedures are followed after visualization procedure.

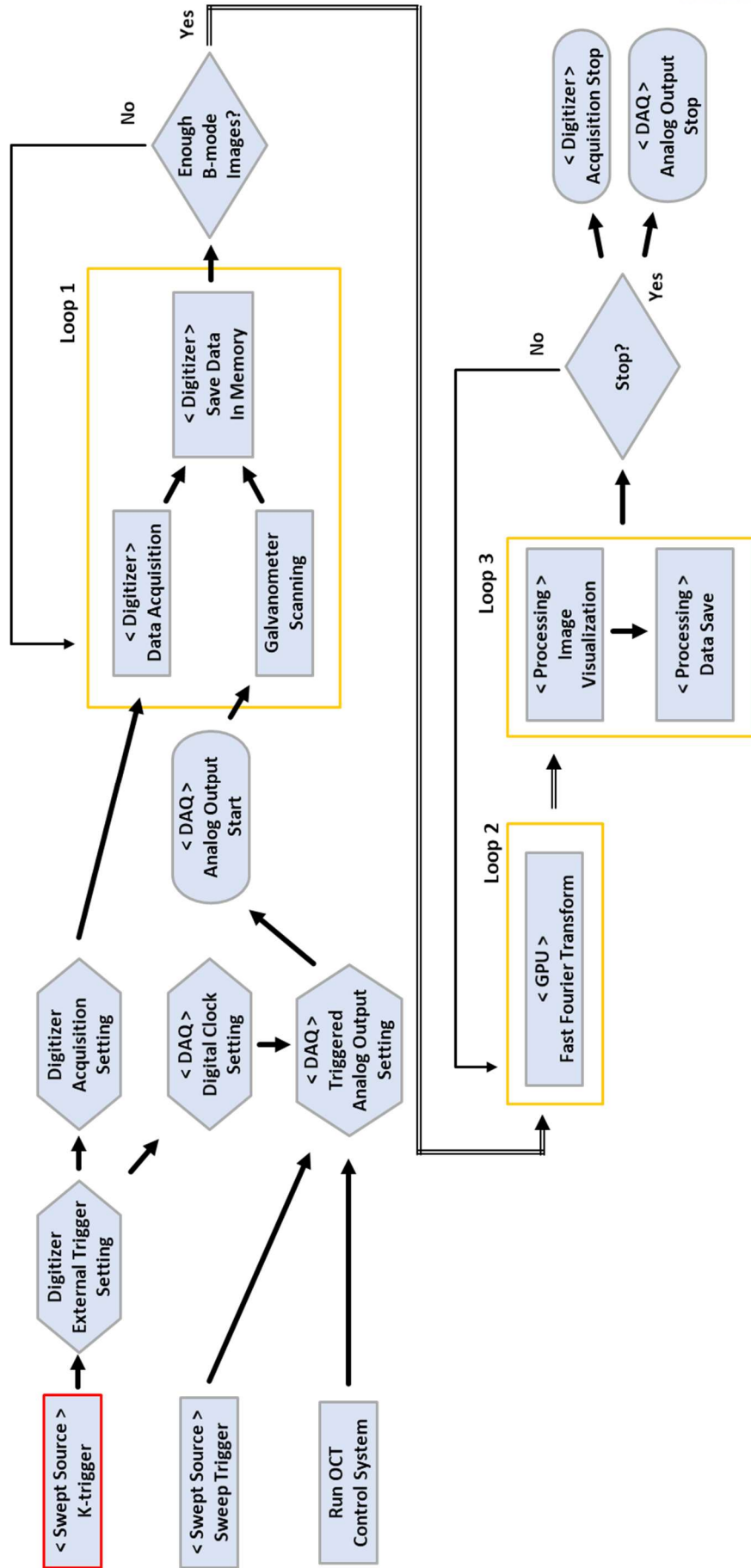


Figure 2.13 Operation algorithm for swept source OCT

3. System Development

Based on the developed SD-OCT and SS-OCT, versatile scanning methods are applied to enhance imaging depth. Two different type of scanning apparatus called co-axial vertical scanning OCT and circular scanning OCT are developed. Those scanning methods are adaptable to all different type of OCT system since scanning method is independent from interferometer and detector. The detailed information about each scanning method will be followed.

3.1. Co-axial Vertical Scanning OCT

The co-axial vertical scanning OCT (CVS-OCT) is designed to provide dual imaging plane using several simple optical components. The CVS-OCT utilizes metal coated prisms to separate single scanning beams and deliver each top and bottom of sample. The co-axial vertical scanner consists of collimator, dual-axis galvanomirror, focusing lens and metal coated prisms. The dual-axis galvanomirror scans laser beam within given range after pass focusing lens. The center metal coated prism can physically divide scan range into two opposite direction and other prisms guide each scan beam to top and bottom of sample respectively. The separated laser beams can reach co-axial position at vertical section of sample. The reflected beam from the sample also follows the same optical pathway and coupled with reference beam at a fiber coupler.

3.1.1. Hardware Setup

For the experiment, the co-axial scanner is combined with 1310 nm SS-OCT system as described in previous section. Since the dual scanning part requires simple optical components, it is possible to develop scanner as hand-held type as shown in Figure 3.1. Five different prisms are held at a given distance with guiding plate. The external probe shell is designed to hold galvanoscanner and collimator, focusing lens are fixed using 3D printer. The physical dimension of probe is 15cm by 15cm. The scanning motion of co-axial scanner can be visualized through 650nm wavelength laser source.

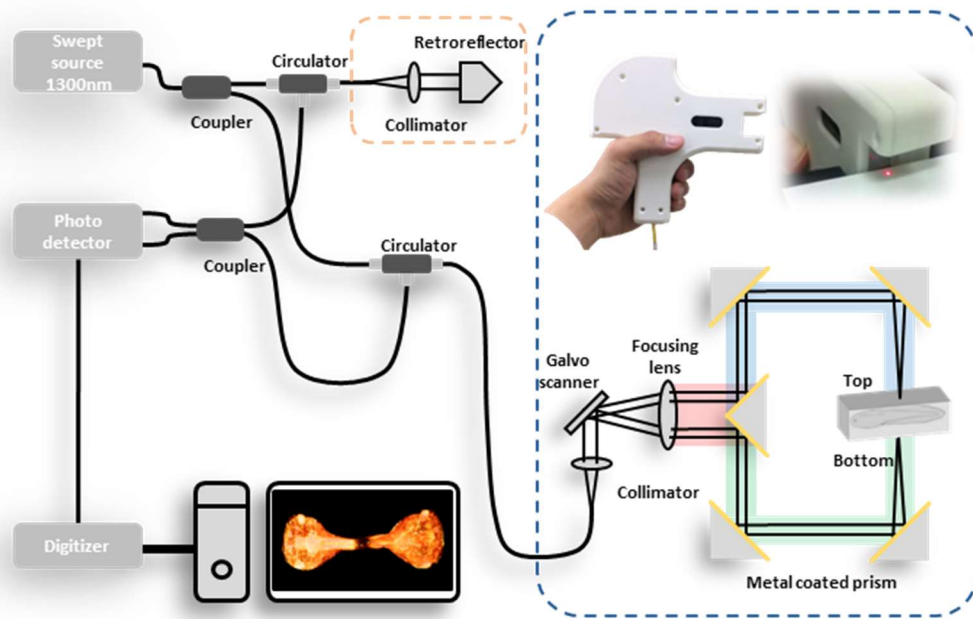


Figure 3.1 System schematics for co-axial vertical scanning OCT

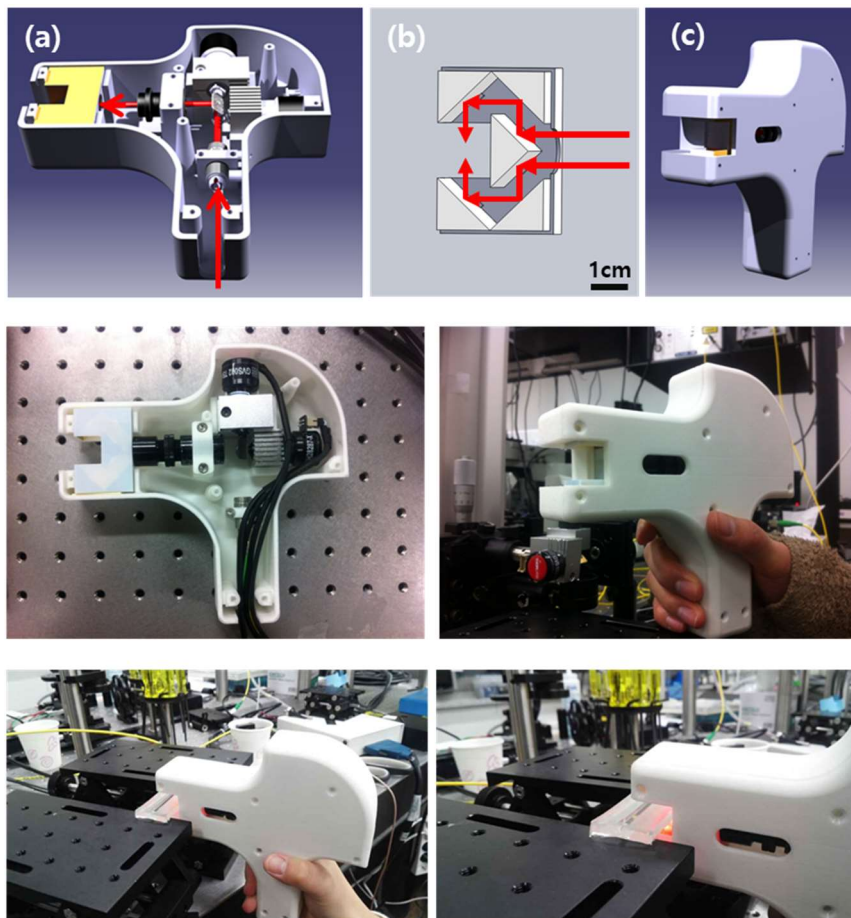


Figure 3.2 Hand-held type scanner of co-axial vertical scanning probe

3.1.2. Image Calibration

Since cross sectional image is acquired through CVS-OCT, top and bottom images should be combined as single cross-sectional image. However, divided images are not in same coordination in depth direction and enface plane due to the physical error of mirror alignment in co-axial vertical scanner. To compensate displacement of top and bottom view, grid patterned film was used as described in Figure 3.3. The following image merging procedures can be categorized in two parts, XY axis correction and Z axis correction.

The co-axial vertical imaging was performed on calibration film layer first to align and merge top and bottom view together. The calibration film layer was composed of five sheets, as a series of plastic tape, grid film, glue, grid film and plastic tape. The grid was printed with laser printer on transparent plastic sheet. Each grid has 1mm pitch with thick line at every 5mm on vertical and horizontal direction to identify origin of grid. The result image of calibration film was utilized to compensate coordination shifting of top and bottom images.

The cross-section image of calibration film has 5 different layers and is represented on left and right of input image. Since there exist same thick line at top and bottom images, we can recognize that the two images are acquired at same position. After dividing left and right images, they are stacked and averaged to acquire enface projection image. It is possible to extract vertical and horizontal grid line based on binary filter and linear interpolation. By extracting grids from averaged enface image, cross points and origin can be identified where thin and thick lines cross over. To match displacement of XY plane, the coordination information of cross points is utilized. By applying affine transformation matrix with corresponding cross points of top and bottom grid images, we could compensate rotation and shifting on XY plan.

After enface correction, modified cross section images are generated from stacked image buffer. To align Z direction, we calculated auto-correlation between every A-line profile of top and bottom. At the index of maximum correlation value as the best match index, separated images are shifted and combined through summation of weighted intensity across depth and normalization of image intensity. Based on the calibration coefficients acquired through above algorithm, other sample images can be merged as single image.

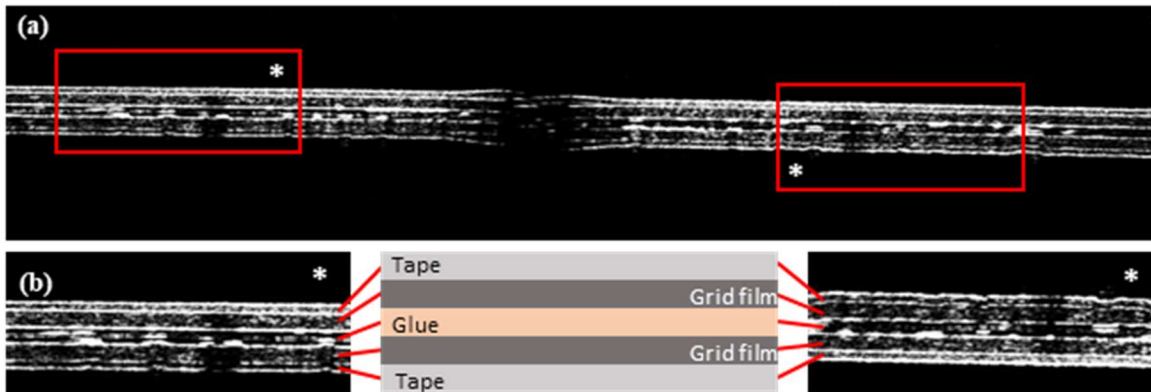


Figure 3.3 Calibration film for co-axial vertical scanning OCT

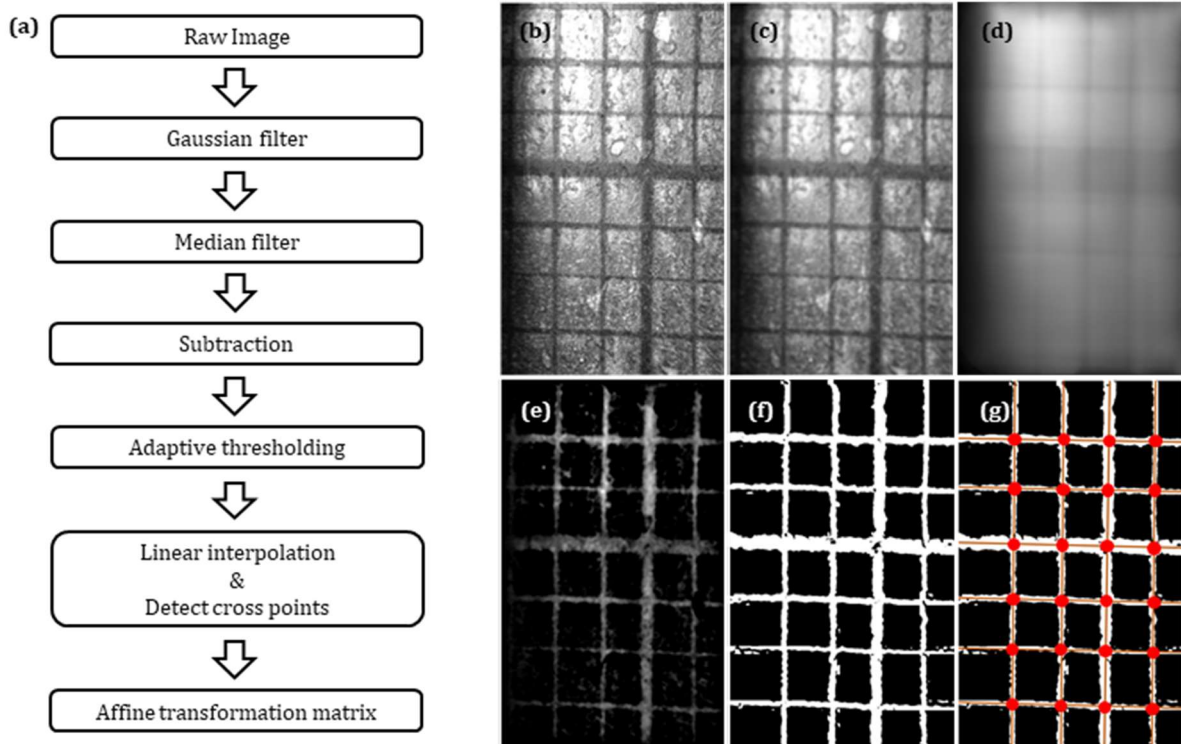


Figure 3.4 Algorithm for mapping top and bottom images

3.2. Circular scanning OCT

Conventional dual axis galvanomirror has its inborn scanning distortion since first reflected beam from first scanning axis cannot meet the exact pivoting point of second scanner. The scanning distortion gives no big trouble in conventional OCT system due to its independent scan motion. However, if the scanning beam generates circular shape, two different scanning axes start to have sine and cosine relationship. The two axes dependent motion could generate severe distortion of scanning motion giving ellipsoidal shape despite circular control signal. To remove scanning distortion during galvanomirror scanning, paired lens was used to focus scanning beam onto pivoting point of another scanning axis as shown in **Figure 3.5**.

3.2.1. Hardware Setup

The key component for the circular scanning OCT is truncated cone shape mirror with metal coating on slope side. When the circular scanning beam hits the metal coated mirror, it reflects beam onto orthogonal direction of sample that is inserted into the hole of mirror. Although the 3-dimensional scanning motion of conventional OCT was done by one of dual axis scanner, the circular scanning OCT utilizes dual axis scanner together for a single scan, and thus, needs additional actuator to generate C-scan motion. Although it can scan horizontal direction of sample by enlarging or minimizing the diameter of circular scan, that could give another distortion factor for reconstructing 3-dimensional image. The C-scan with linear stage was tested on the conventional OCT scanner, and it can clearly reject additional image distortion such as aberration as shown in **Figure 3.6**. The additional linear stage can help C-scan motion of circular scanning OCT by moving a step distance after a circular scan. In **Figure 3.7**, the system was demonstrated with character printed pen to generate 3-dimensional structure of it. After 3-dimensional reconstruction of sample, the character is preserved as its own shape.

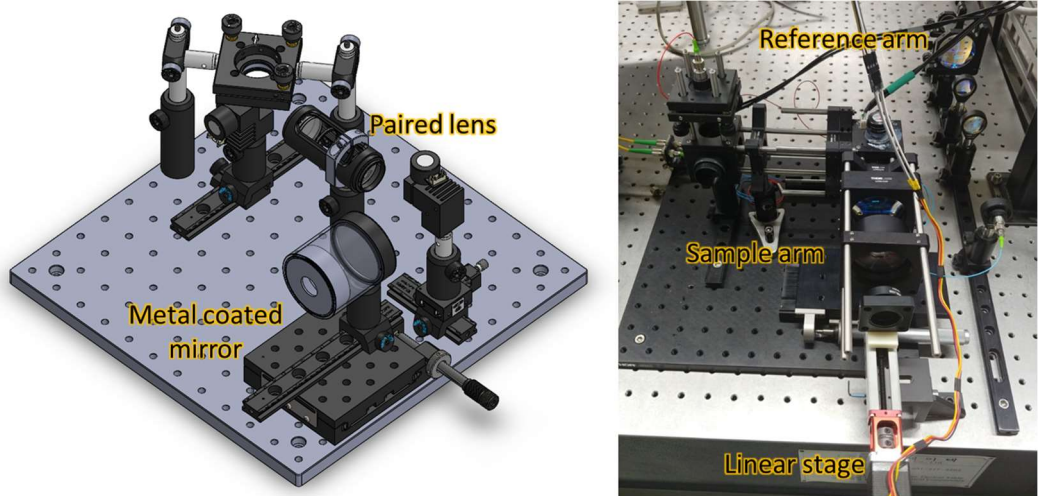


Figure 3.5 Schematic diagram for circular scanning OCT and real.

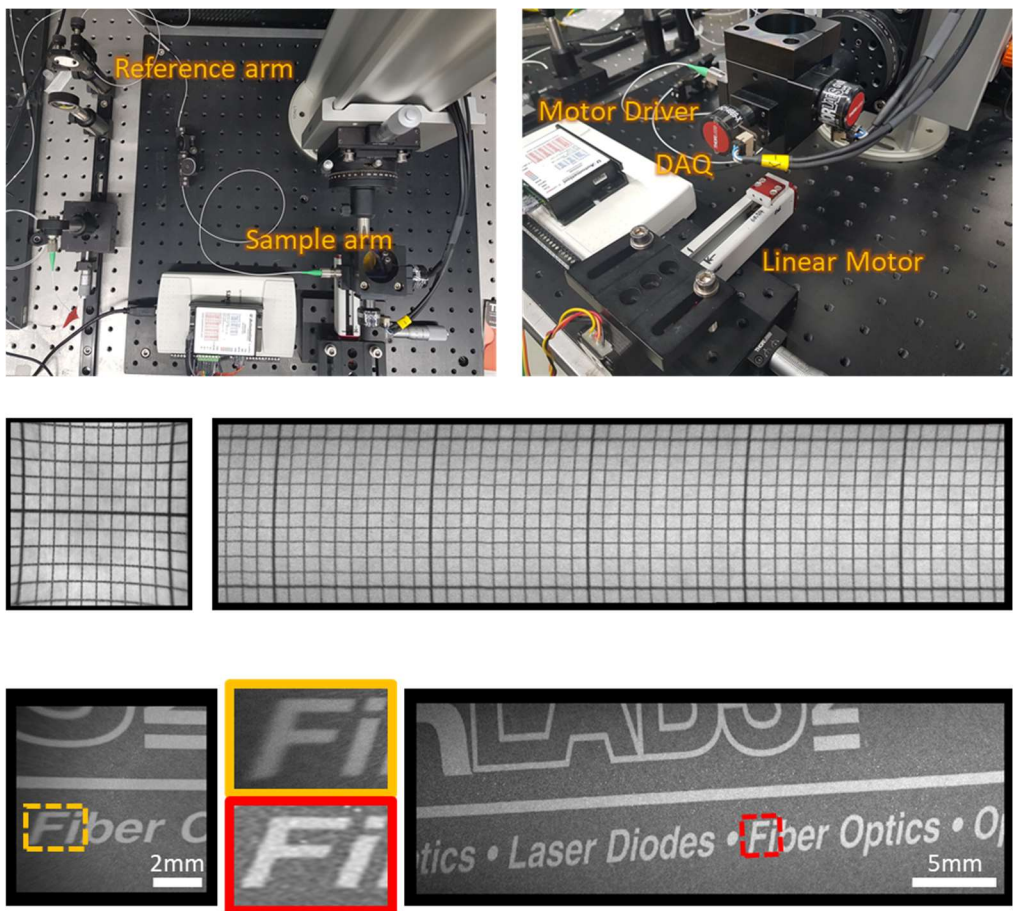


Figure 3.6 Comparison of conventional and linear scanning system

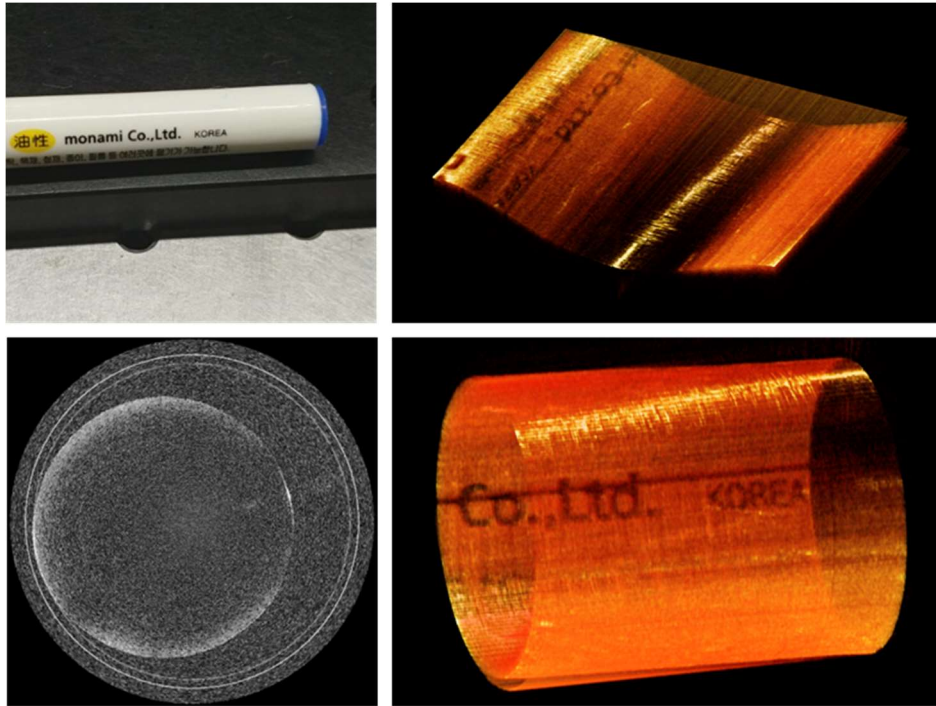


Figure 3.7 3D reconstructed image of pen through circular scanning OCT

3.2.2. Image Reconstruction

When the signal is acquired and visualized through OCT software, the cross-section image comes with flatten shape since image is generated based on optical distance, not a physical distance. To visualize real tomographic image, flatten image with cartesian coordination needs to be transformed into polar coordination. Although after the conversion of polar coordination, the circular image should also be represented in (x', y') cartesian coordination. Thus, the coordination need to be convert twice as polar conversion (r, θ) of flat image (x, y) and cartesian conversion (x', y') of circular image.

For the first, the flat image can be reconstructed as circular image by interpreting a radius value to y value, θ value to the current position ratio of B-scan times 360 degree. Then, wrapped circular image with polar coordination is converted into cartesian coordination through sine and cosine transformation as followed. Finally, single point of flat image can be matched with corresponding point of circular image by simple index rearrange map in **Figure 3.8**.

$$r = y$$

$$\theta = \frac{x}{\#of A_scan} \cdot 2\pi$$

$$x' = r \cdot \cos \theta = y \cdot \cos \left(\frac{x}{\#of A_scan} \cdot 2\pi \right)$$

$$y' = r \cdot \sin \theta = y \cdot \sin \left(\frac{x}{\#of A_scan} \cdot 2\pi \right)$$

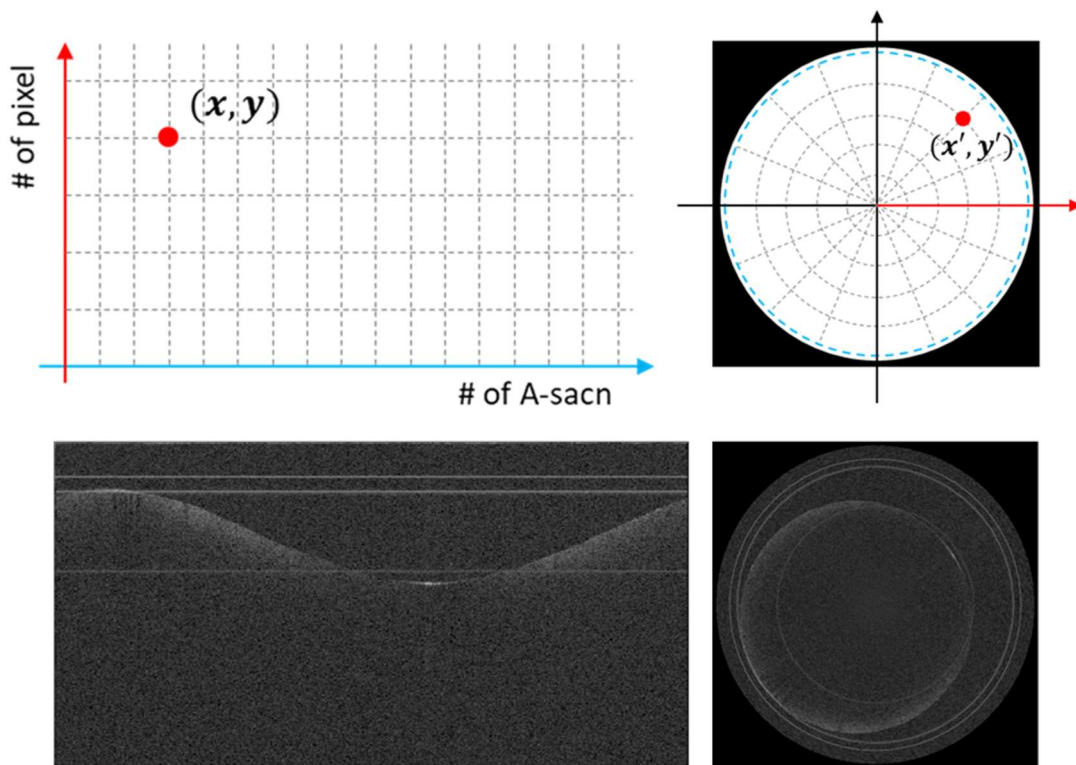


Figure 3.8 Coordination conversion for circular scanning OCT

4. Application

We demonstrated the developed versatile scanning OCT system using various biological samples which have different size, contrast and shape. Especially, 1) volumetric quantification of wound on engineered skin, 2) monitoring an organogenesis of tadpole during developmental procedure, 3) monitoring the overall developmental procedure of Zebrafish, and 4) volumetric visualization of spinal cord and quantification of its defects.

4.1. Quantification of Engineered Skin

During a research for quantitative analysis of wound healing procedure, we monitored laser irradiated artificial skin using OCT [13]. In the **Figure 4.1**, the 3-dimensional reconstructed image shows clear holes on the surface of engineered skin, however, some of those have ambiguous boundary in deep region. Since the boundary of hole is not clear in deep side, it results errors after segmentation of wound. For this reason, we applied co-axial vertical scanner to provide clear boundary of hole at entire depth.

The single side scanning of co-axials scanner can visualize only top or bottom surface of artificial skin, resulting ambiguous boundary information of laser irradiated hole. It was impossible to segment out defect region only with single side view. After applying the suggested alignment algorithm in **section 3.1.2**, the separated artificial skin images can be merged as one. The merged image shows better contrast of hole comparing to the single image in **Figure 4.2**. Based on the intensity and morphology, the wound part successfully segmented out as represented in red-color providing quantitative volume information of wound.

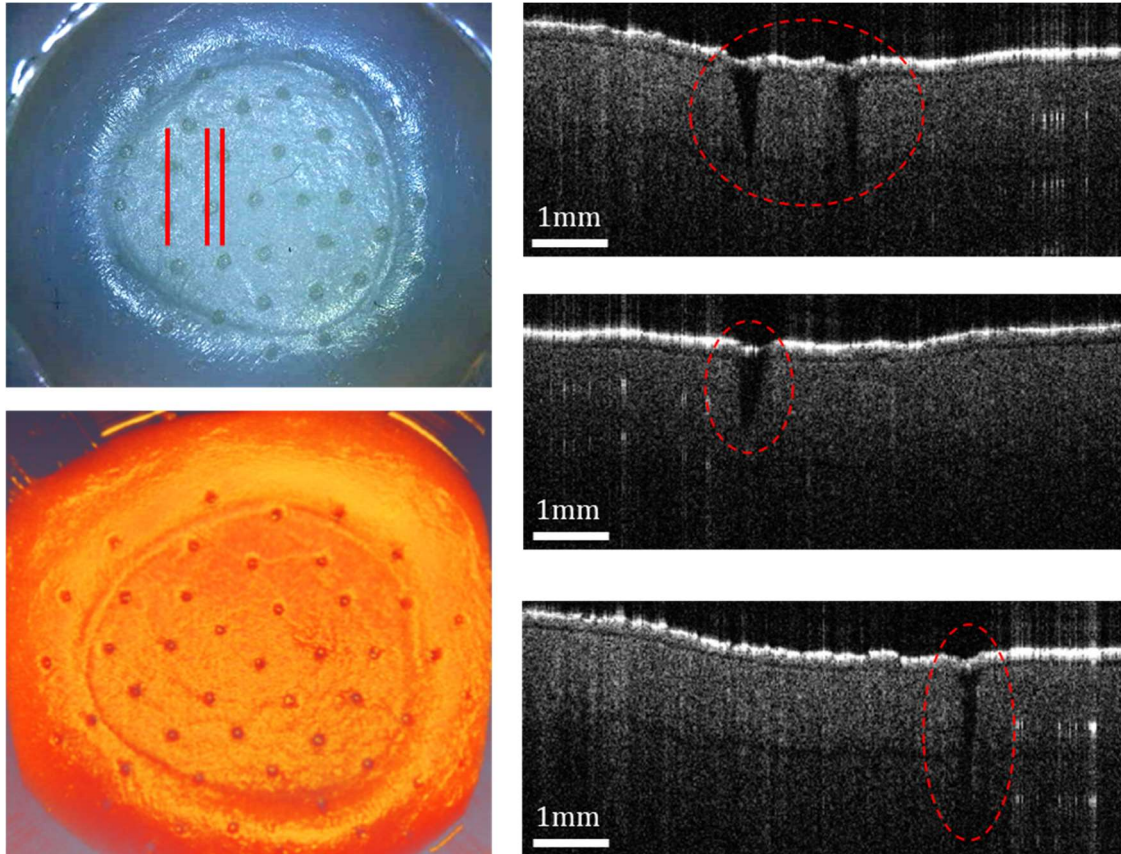


Figure 4.1 3D reconstructed image and cross-section image of engineered skin

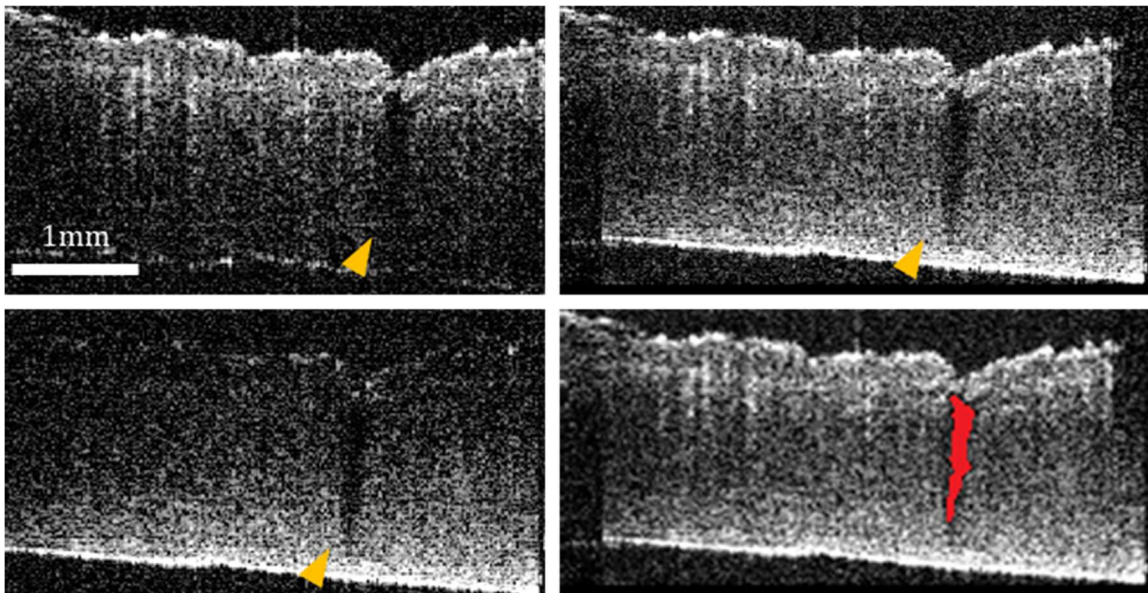


Figure 4.2 Merged image of top and bottom and segmentation of wound region

4.2. Monitoring of Tadpole Development

Since OCT can visualize endogenous contrast of live sample, OCT helps developmental study to analyze microstructure changes in embryonic animal models. The 800nm SD-OCT system was applied to monitor developmental procedure of *Xenopus larvae* from early stage to stage 47. Interestingly, the physical property of tadpole embryo changes dramatically according to the stage of developmental procedure. In the stage of oocyte, it is transparent so that the normal optical microscopy can visualize whole structure. However, as the stage goes further, the tadpole embryo becomes opaque and is impossible to acquire tomographic image through OCT as shown in **Figure 4.3** [35]. After specific stage around 25, it starts to become transparent again, providing deeper cross-section information. Thus, conventional OCT scanner only can visualize whole body information of limited stage of tadpole.

To overcome the depth limitation, co-axial vertical scanning OCT (CVS-OCT) was used providing whole body 3-dimensional structure of *Xenopus Larvae* at stage 47 in **Figure 4.4**. Although the sample is transparent enough, it is hard to visualized entire structure of tadpole at late stage due to the size of embryo. Even the sample is held with slightly tilt position, the CVS-OCT can acquire clear image of each organ inside of embryo. The whirlpool shape of gut and gland under the eye also can be visualized and segmented out clearly.

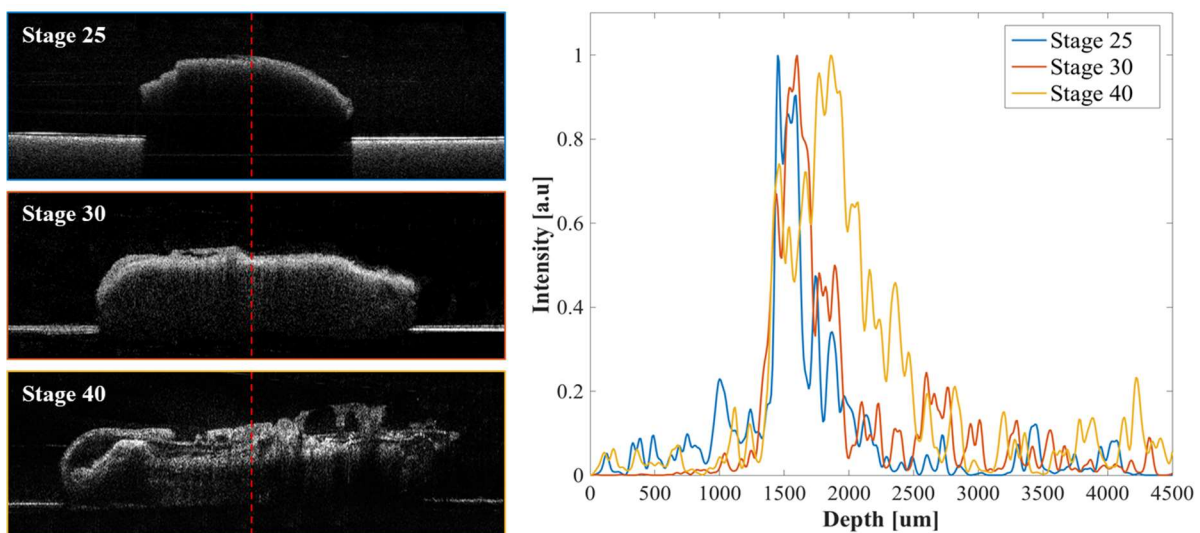


Figure 4.3 Tomographic image of tadpole embryo and A-line profile at different stage.

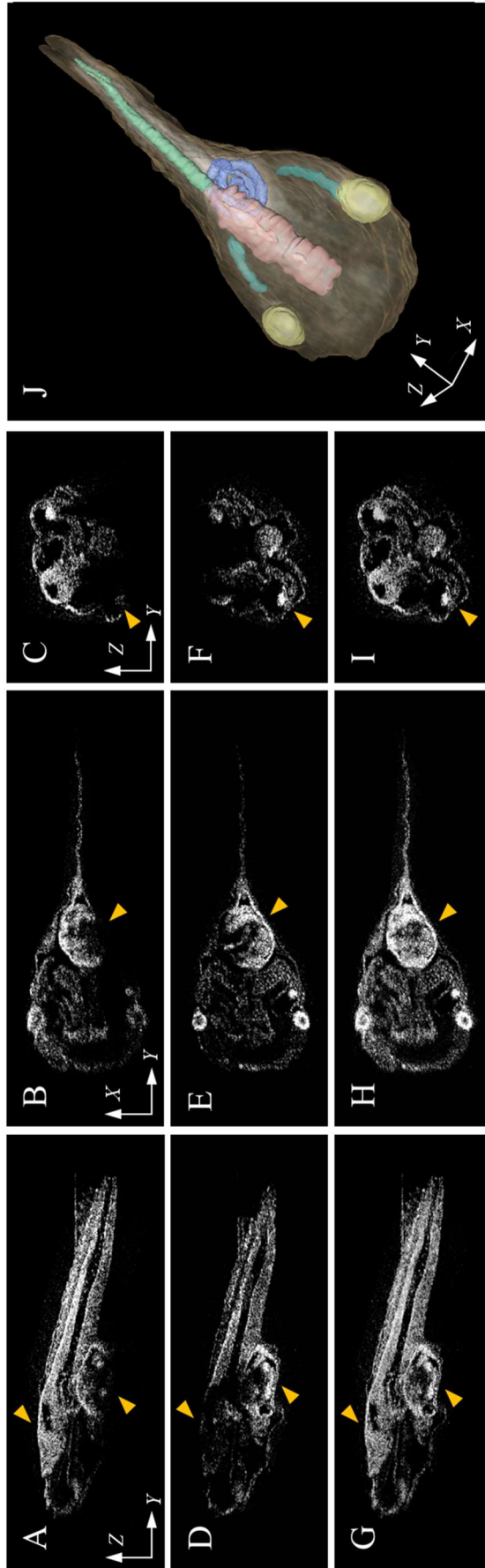


Figure 4.4 Volumetric analysis of *Xenopus laevis*

4.3. Monitoring of Zebrafish Development

The zebrafish has been an important animal model for biomedical research due to its fast life cycle, simple optical access and fully sequenced genome information [36-39]. The number of eggs after fertilization also help researchers to experiment efficiently. Meanwhile, according to the Mendel's law, not all the eggs express target mutated genes. Thus, researchers should have to check every single sample through microscopy to screen out targeted phenotype, which costs lots of time and effort.

To solve the phenotype screening problem, conventional OCT and co-axial vertical scanning OCT was applied. For OCT imaging, the zebrafish is embedded into customized microfluidic channels which holds single sample on single line. Since the fixed sample has dark imaging contrast at yolk site, all the zebrafishes are monitored in live state. Using a Tricaine methanesulfonate, as an anesthesia agent, the movement of zebrafish can be blocked [40]. After sample preparation, the microfluidic channel is placed under the scanner. Through the OCT, the morphogenesis of a heart can be clearly monitored at pfh48. Since the imaging speed of OCT was reduced for large number of A-line scan, small fluctuation of heart motion was recorded in **Figure 4.5**. The monitored zebrafish has inborn fluorescence of mCherry and GFP. To figure out developmental difference between control and fluorescence mutated zebrafish, both are monitored during 120pfh and shows no significant differences in **Figure 4.6**.

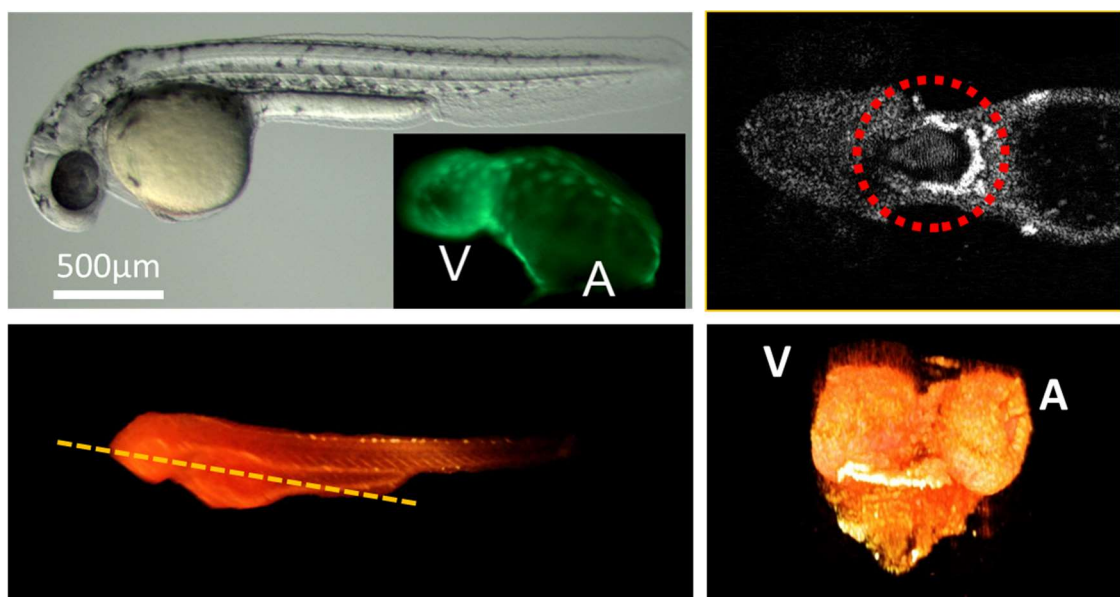


Figure 4.5 Visualization of Zebrafish and its heart at 48pfh

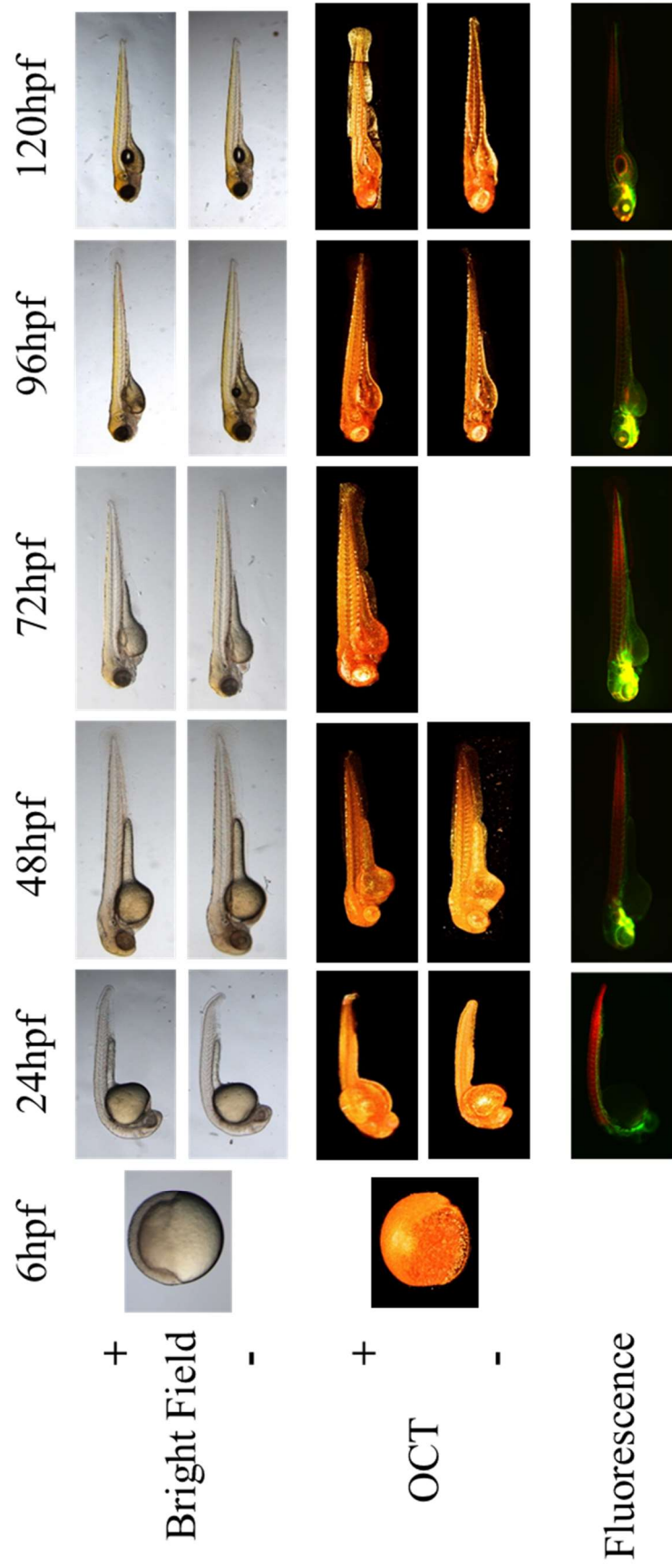


Figure 4.6 Developmental monitoring of Zebrafish using various imaging techniques

4.4. Quantification of Spinal Cord Injury

Quantification of spinal cord injury (SCI) is important for correlation of defect site and its behavior. Over past decades, various treatment including medication, physical surgery, rehabilitation therapy and stem cell treatment for SCI have been studied to regenerate injured spinal cord [41-45]. There exist only few ways to visualize spinal cord optically such as confocal and multi-photon microscopy [46]. Although these imaging technologies provide high resolution information, the imaging depth of them is limited in several hundreds of micrometers. Thus, we tried to visualize endogenous contrast for spinal cord through circular scanning OCT.

- **Contrast enhancement**

Before the circular scanning OCT, we analyzed morphology of mouse spinal cord. For the common methodology to visualize cross section of biological tissue, the histology with chemical staining has been widely used. The spinal cord has two distinct morphology called white matter (WM) and gray matter (GM) and it is hard to distinguish those two with naked eye. As a well-known staining method, the haematoxylin and eosin (H&E) was applied to see the difference of WM and GM in **Figure 4.7** [47]. Since the H&E only can stain cytoplasm and nucleus, it cannot give dynamic contrast. Meanwhile, the luxol fast blue (LFB) selectively stains myelin which covers axon, resulting dark blue staining at fiber rich WM.

After then, we tried to visualize cross-section of mouse spinal cord through high-resolution optical coherence microscopy (OCT) system with 10x objective lens. Since the field-of-view for high magnification lens is limited, multiple mosaic images of spinal cord were stitched into single enface image as shown in **Figure 4.8**. The optical contrast for spinal cord is good enough to distinguish WM and GM due to different optical scattering of them. For further contrast enhancement, another technique called tissue clearing can be adapted with OCM. The clearing agent, called Scale2, could change physical transparency of biological tissue by filling space of internal structure with given chemical components [48]. Thereafter, we could acquire relatively less optical scattering from WM giving dynamic contrast difference between WM and GM.

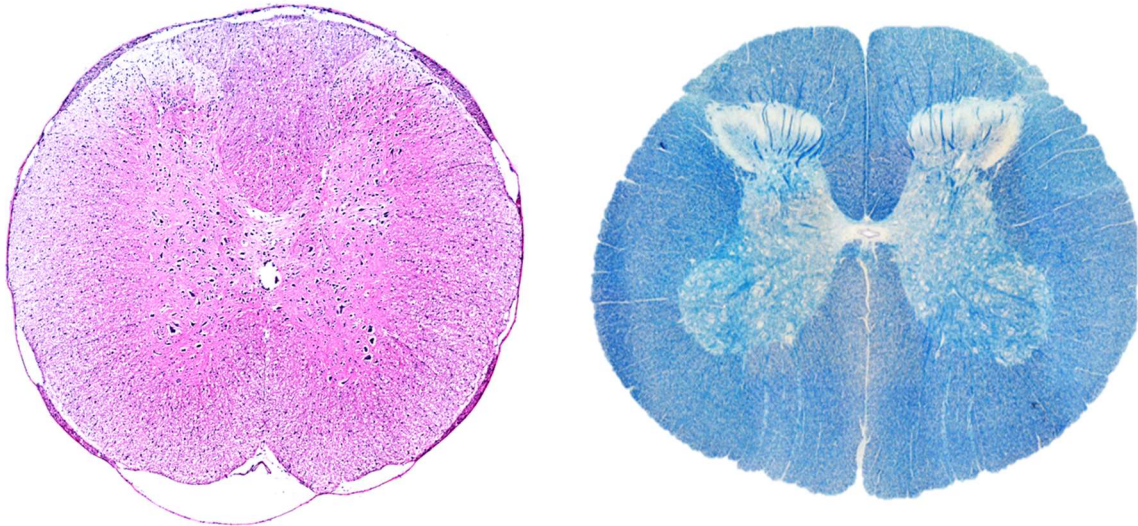


Figure 4.7 Histology of mouse spinal cord stained with H&E and LFB

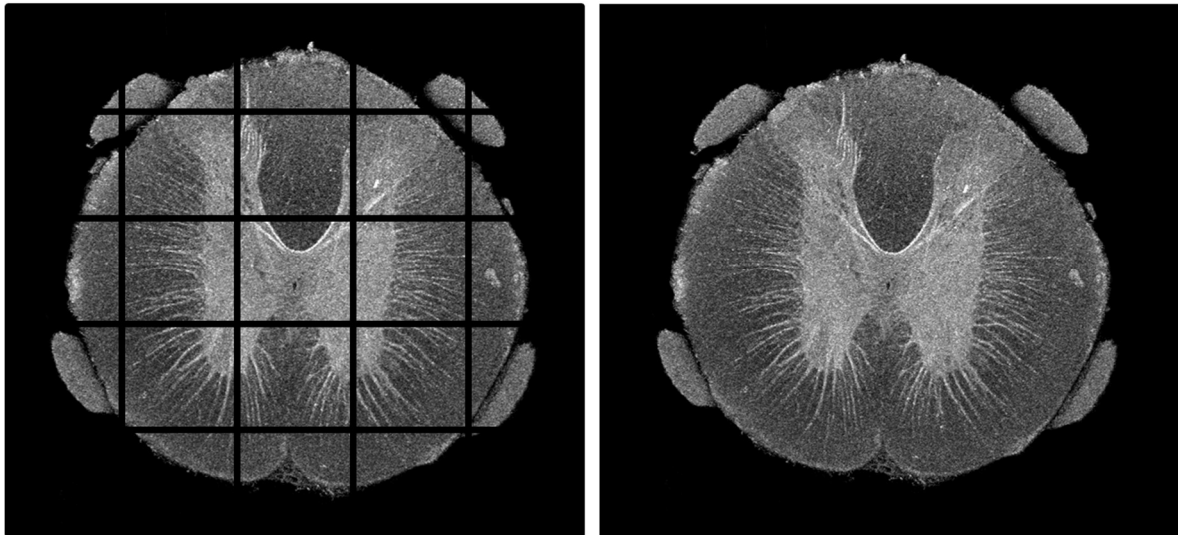


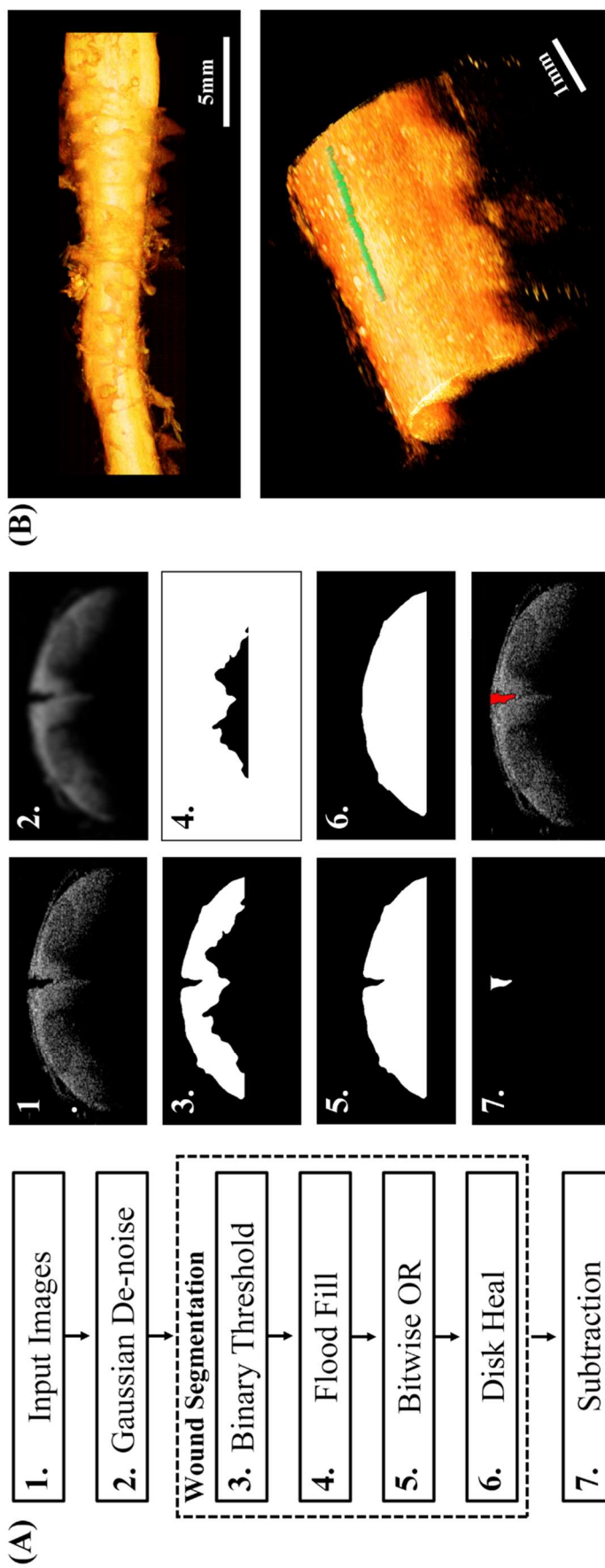
Figure 4.8 Cross-sectional demonstration of mouse spinal cord using OCM

- **SCI Quantification Algorithm**

For quantification of spinal cord injury (SCI), we developed algorithm which can be applied in normal OCT image and circular OCT image as represented in **Figure 4.9**. To make SCI model, small portion of spinal cord from mice was drilled out [49]. Using linear actuator and galvanomirror, total 25mm length of spinal cord images were saved.

Since OCT acquires randomly scattered light from tissue, random speckle noise comes with tomography image. The random noise may affect the result of binary filter or subtraction of images. To reject the noise, Gaussian filter was adapted providing smoothen image with preserved injury boundary. After binary threshold, the spinal cord region is isolated with unexpected drooping surface of bottom. Before subtraction of defect reseed image and defect filled image, other differences except injury region should be rejected to acquire only wound area. Through the flood fill method, the drooping surface at the bottom of isolated spinal cord can be filled as flat bottom surface.

While extract the injury area on the surface of spinal cord, the opened shape of defect should be closed first with expected surface line. To expect the surface line, we applied disk heal algorithm which detects sudden drop of line and compensate with circular curved line. Finally, we acquired two different images including defect conserved image and defect. Through simple subtraction between two images, defect area is clearly segmented. Within a given length of spinal cord, we could separate and quantify the volumetric size of injury. Although the algorithm figure represents conventional OCT images, the suggested algorithm can be also applied to the image of circular scanning OCT.



- **Circular Imaging**

For circular imaging of a sample, it is important to hold a sample on the central axis of cylindrical imaging plane without any free movement. To prepare spinal cord for circular imaging, 1ml syringe and agarose are used in **Figure 4.10**. The external grid and characters of a syringe can be easily removed by sticky tape. After then, pull the liquid state of 4% low melting point agarose and put small part of spinal cord and fix the center position before gelation. While holding a spinal cord on the center of syringe, carefully remove all vapors inside of agarose gel (b, c).

When the syringe is ready for imaging, hold it onto the linear stage and gently change the angle so that OCT image become flat. The flat surface of syringe represents on-axis of circular scan. After setting center position, move metal coated mirror toward objective lens so that lasers focus on to the surface of spinal cord. Since the spinal cord is not exact circular shape, there exist fluctuation of cross-section image. If the spinal cord is visible, re-arrange reference length until it matches with optical path length of sample arm. Finally, the linear stage moves along the central axis of cylindrical imaging plane, providing 3-dimensional volumetric image of spinal cord.

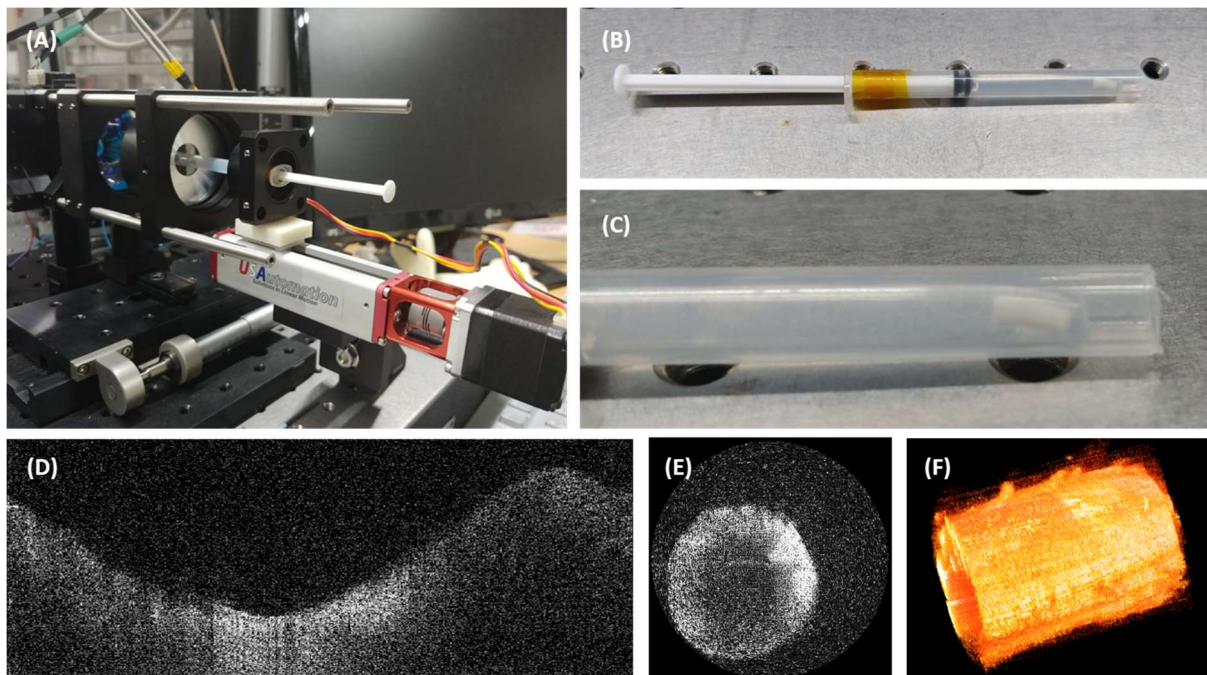


Figure 4.10 Sample preparation of spinal cord and 3D reconstructed image

5. Discussion and Conclusion

▪ Co-axial vertical scanning OCT

Through the above studies in **section 4.1 - 4.3**, the dual sided imaging plane of CVS-OCT was successfully demonstrated with engineered skin, tadpole and zebrafish. For the thick sample, less than twice of the penetration depth can be visualized clearly after merging the top and bottom images. Even small part of organs can be segmented out with preserved image contrast.

After the developmental study of zebrafish, we fully understood the necessity of the screening system for phenotype at early stage of development. Since the CVS-OCT divides single stroke of scan to the top and bottom, the imaging area is limited to the 7mm by 15mm, resulting almost single sample at single scan. Also, long focal length of objective lens limits detailed structure of embryo of tadpole and zebrafish. The resolution is not enough to differentiate the structural variation of blood vessel in the mutated embryo as shown in **Figure 5.1** right [36]. Thus, the CVS-OCT system need to be modified with high NA objective lens and large field of view. Since high magnification objective lens has small scan range, multiple prism may not divide and deliver correctly. Therefore, physically independent two scanners should be applied to generate entire volumetric structure.

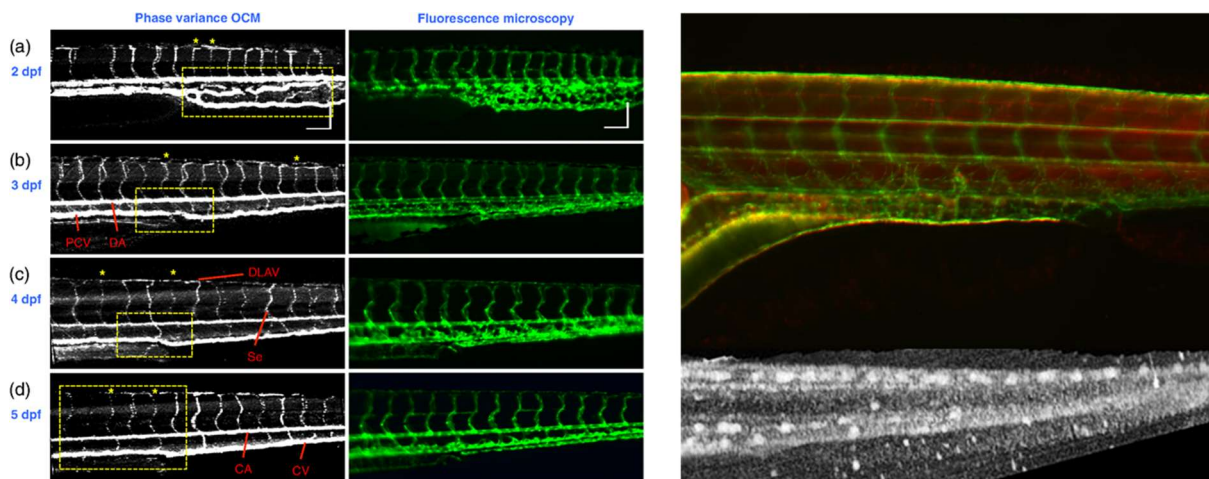


Figure 5.1 Visualization of vascular deformation using OCT and fluorescence microscope

- **Circular scanning OCT**

The circular scanning OCT can visualize clear surface structure of cylindrical sample as demonstrated in **section 3.2**. Since the phantom has perfect circular tube shape, the polar reconstructed image shows circular shape of surface. For the additional application, the circular scanning OCT can be applied to 3-dimensional scanner for microstructure of small sample. Since OCT acquire out-most and internal structure together, it can be a solution for multi-layer structure object scanner.

Although the imaging window was fully utilized by reflecting laser beam orthogonal to the curved sample, it is hard to acquire entire depth information when the sample is not in a perfect cylindrical shape or out of axis. Also, the long focal length results relatively poor imaging resolution comparing to the conventional OCT scanner. The best solution that we could effectively enhance the imaging window is full-range method [50-51]. The full-range method needs phase modulation in acquired signal, and it can be simulated through arbitral noise signal with sinusoidal waveform as shown in **Figure 5.2**. If we can give additional phase through shifting the reference mirror, we can reject the conjugated image from Fourier transformed data. The procedure can be simplified as multiple Fourier transform and Heaviside step function in **Figure 5.3**. Therefore, if the full-range method can be applied in circular scanning OCT, the ellipsoidal shape or out-of-axis sample will be captured without any flipped images. Not only for the circular scanner, but also co-axial scanner can acquire more dynamic structure of sample through suggested full-range method.

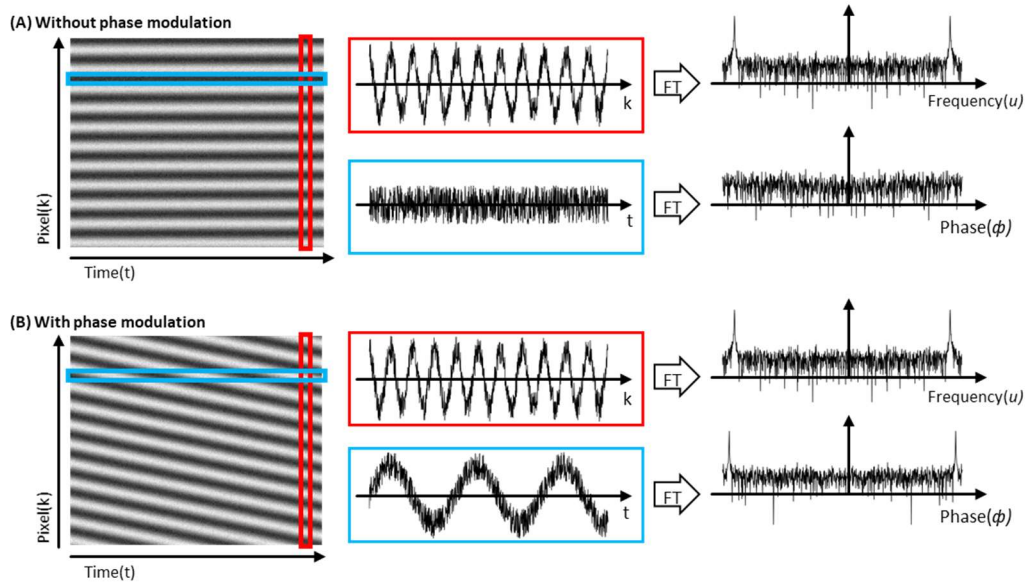


Figure 5.2 Simulation of full-range application with additional phase modulation

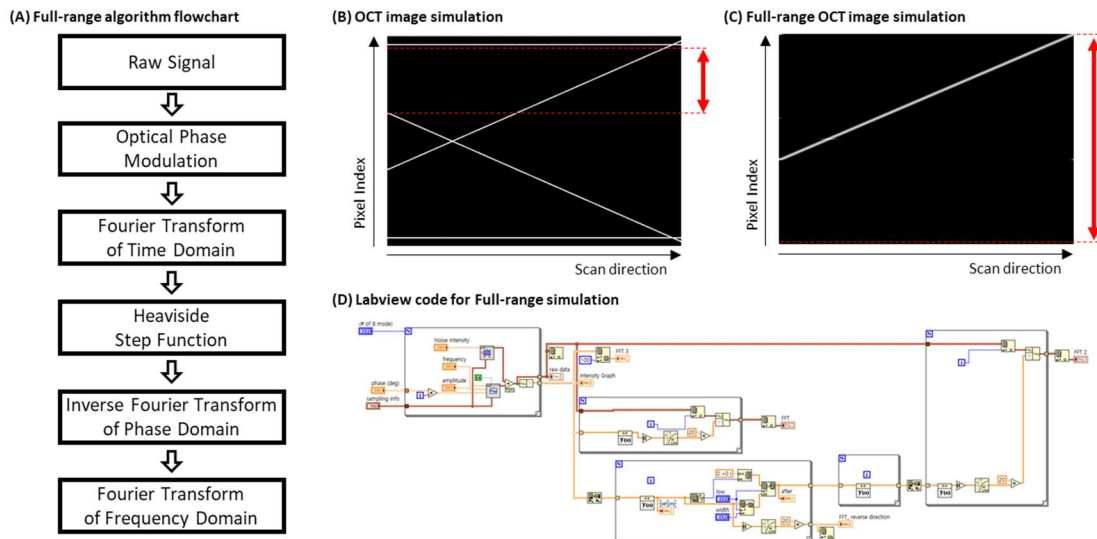


Figure 5.3 Flow-chart and code for full-range algorithm

REFERENCES

1. Tearney, G. J.; Kang, D., Introduction to biomedical optical imaging. *Lasers Surg Med* **2017**, *49* (3), 214.
2. Singh, M.; Wu, C.; Mayerich, D.; Dickinson, M. E.; Larina, I. V.; Larin, K. V., Multimodal embryonic imaging using optical coherence tomography, selective plane illumination microscopy, and optical projection tomography. *Conf Proc IEEE Eng Med Biol Soc* **2016**, *2016*, 3922-3925.
3. Sharpe, J., Optical projection tomography as a new tool for studying embryo anatomy. *J Anat* **2003**, *202* (2), 175-81.
4. Huang, D.; Swanson, E. A.; Lin, C. P.; Schuman, J. S.; Stinson, W. G.; Chang, W.; Hee, M. R.; Flotte, T.; Gregory, K.; Puliafito, C. A.; et al., Optical coherence tomography. *Science* **1991**, *254* (5035), 1178-81.
5. Stelzer, E. H., Light-sheet fluorescence microscopy for quantitative biology. *Nat Methods* **2015**, *12* (1), 23-6.
6. Pampaloni, F.; Chang, B. J.; Stelzer, E. H., Light sheet-based fluorescence microscopy (LSFM) for the quantitative imaging of cells and tissues. *Cell Tissue Res* **2015**, *360* (1), 129-41.
7. Huang, Y.; Liu, X.; Kang, J. U., Real-time 3D and 4D Fourier domain Doppler optical coherence tomography based on dual graphics processing units. *Biomed Opt Express* **2012**, *3* (9), 2162-74.
8. Kobayashi, M.; Haraguchi, Y.; Shimizu, T.; Mizuuchi, K.; Iseki, H., Real-time, noninvasive optical coherence tomography of cross-sectional living cell-sheets in vitro and in vivo. *J Biomed Mater Res B Appl Biomater* **2015**, *103* (6), 1267-73.
9. Fu, Q.; Martin, B. L.; Matus, D. Q.; Gao, L., Imaging multicellular specimens with real-time optimized tiling light-sheet selective plane illumination microscopy. *Nat Commun* **2016**, *7*, 11088.
10. Fercher, A. F., Optical coherence tomography—development, principles, applications. *Zeitschrift für Medizinische Physik* **2010**, *20* (4), 251-276.
11. Fan, Y.; Zhang, B.; Chang, W.; Zhang, X.; Liao, H., A novel integration of spectral-domain optical-coherence-tomography and laser-ablation system for precision treatment. *Int J Comput Assist Radiol Surg* **2017**.
12. Tang, Q.; Wang, J.; Frank, A.; Lin, J.; Li, Z.; Chen, C. W.; Jin, L.; Wu, T.; Greenwald, B. D.; Mashimo, H.; Chen, Y., Depth-resolved imaging of colon tumor using optical coherence tomography and fluorescence laminar optical tomography. *Biomed Opt Express* **2016**, *7* (12), 5218-5232.

13. Ahn, Y.; Lee, C. Y.; Baek, S.; Kim, T.; Kim, P.; Lee, S.; Min, D.; Lee, H.; Kim, J.; Jung, W., Quantitative monitoring of laser-treated engineered skin using optical coherence tomography. *Biomed Opt Express* **2016**, *7* (3), 1030-41.
14. Liu, C. H.; Kao, L. Y.; Sun, M. H.; Wu, W. C.; Chen, H. S., Retinal Vessel Density in Optical Coherence Tomography Angiography in Optic Atrophy after Nonarteritic Anterior Ischemic Optic Neuropathy. *J Ophthalmol* **2017**, *2017*, 9632647.
15. Min, E.; Lee, J.; Vavilin, A.; Jung, S.; Shin, S.; Kim, J.; Jung, W., Wide-field optical coherence microscopy of the mouse brain slice. *Opt Lett* **2015**, *40* (19), 4420-3.
16. Kim, J.; Dave, D. P.; Rylander, C. G.; Oh, J.; Milner, T. E., Spatial refractive index measurement of porcine artery using differential phase optical coherence microscopy. *Lasers Surg Med* **2006**, *38* (10), 955-9.
17. Gigan, S., Optical microscopy aims deep. *NATURE PHOTONICS* **2017**, *11*, 14-16.
18. Richardson, D. S.; Lichtman, J. W., SnapShot: Tissue Clearing. *Cell* **2017**, *171* (2), 496-496 e1.
19. Alex, A.; Povazay, B.; Hofer, B.; Popov, S.; Glittenberg, C.; Binder, S.; Drexler, W., Multispectral in vivo three-dimensional optical coherence tomography of human skin. *J Biomed Opt* **2010**, *15* (2), 026025.
20. Ding, Z.; Ren, H.; Zhao, Y.; Nelson, J. S.; Chen, Z., High-resolution optical coherence tomography over a large depth range with an axicon lens. *Opt Lett* **2002**, *27* (4), 243-5.
21. Laviers, H.; Zambarakji, H., Enhanced depth imaging-OCT of the choroid: a review of the current literature. *Graefes Arch Clin Exp Ophthalmol* **2014**, *252* (12), 1871-83.
22. Ravichandran, N. K.; Wijesinghe, R. E.; Shirazi, M. F.; Park, K.; Jeon, M.; Jung, W.; Kim, J., Depth enhancement in spectral domain optical coherence tomography using bidirectional imaging modality with a single spectrometer. *J Biomed Opt* **2016**, *21* (7), 76005.
23. Sharma, U.; Chang, E. W.; Yun, S. H., Long-wavelength optical coherence tomography at 1.7 microm for enhanced imaging depth. *Opt Express* **2008**, *16* (24), 19712-23.
24. Wu, C.; Sudheendran, N.; Singh, M.; Larina, I. V.; Dickinson, M. E.; Larin, K. V., Rotational imaging optical coherence tomography for full-body mouse embryonic imaging. *J Biomed Opt* **2016**, *21* (2), 26002.
25. Yu, H.; Jang, J.; Lim, J.; Park, J. H.; Jang, W.; Kim, J. Y.; Park, Y., Depth-enhanced 2-D optical coherence tomography using complex wavefront shaping. *Opt Express* **2014**, *22* (7), 7514-23.

26. McGowan, J. W.; Bidwell, G. L., 3rd, The Use of Ex Vivo Whole-organ Imaging and Quantitative Tissue Histology to Determine the Bio-distribution of Fluorescently Labeled Molecules. *J Vis Exp* **2016**, (118).
27. Yu, H.; Lee, P.; Jo, Y.; Lee, K.; Tuchin, V. V.; Jeong, Y.; Park, Y., Collaborative effects of wavefront shaping and optical clearing agent in optical coherence tomography. *J Biomed Opt* **2016**, *21* (12), 121510.
28. Richardson, D. S.; Lichtman, J. W., Clarifying Tissue Clearing. *Cell* **2015**, *162* (2), 246-257.
29. Watson, T.; Andrews, N.; Davis, S.; Bugeon, L.; Dallman, M. D.; McGinty, J., OPTiM: Optical projection tomography integrated microscope using open-source hardware and software. *PLoS One* **2017**, *12* (7), e0180309.
30. Magsam, A. W.; Johnson, M.; Villani, T.; Pierce, M. C., Optical Projection Tomography with a Tissue Clearing Agent for Developmental and Reproductive Toxicology Studies. *Birth Defects Res* **2017**.
31. Sharpe, J., Optical projection tomography. *Annu Rev Biomed Eng* **2004**, *6*, 209-28.
32. Ford, H. D.; Beddows, R.; Casaubieilh, P.; Tatam*, R. P., Comparative signal-to-noise analysis of fibre-optic based optical coherence tomography systems. *Journal of Modern Optics* **2005**, *52* (14), 1965-1979.
33. Hu, Z.; Rollins, A. M., Fourier domain optical coherence tomography with a linear-in-wavenumber spectrometer. *Opt Lett* **2007**, *32* (24), 3525-7.
34. Jeon, M.; Kim, J.; Jung, U.; Lee, C.; Jung, W.; Boppart, S. A., Full-range k-domain linearization in spectral-domain optical coherence tomography. *Appl Opt* **2011**, *50* (8), 1158-63.
35. Grainger, R. M., *Xenopus tropicalis* as a Model Organism for Genetics and Genomics: Past, Present and Future. *Methods in molecular biology (Clifton, N.J.)* **2012**, *917*, 3-15.
36. Chen, Y.; Trinh, L. A.; Fingler, J.; Fraser, S. E., Phase variance optical coherence microscopy for label-free imaging of the developing vasculature in zebrafish embryos. *J Biomed Opt* **2016**, *21* (12), 126022.
37. Hoo, J. Y.; Kumari, Y.; Shaikh, M. F.; Hue, S. M.; Goh, B. H., Zebrafish: A Versatile Animal Model for Fertility Research. *Biomed Res Int* **2016**, *2016*, 9732780.
38. Chakraborty, C.; Sharma, A. R.; Sharma, G.; Lee, S. S., Zebrafish: A complete animal model to enumerate the nanoparticle toxicity. *J Nanobiotechnology* **2016**, *14* (1), 65.
39. Flinn, L.; Bretaud, S.; Lo, C.; Ingham, P. W.; Bandmann, O., Zebrafish as a new animal model for

- movement disorders. *J Neurochem* **2008**, *106* (5), 1991-7.
40. Matthews, M.; Varga, Z. M., Anesthesia and euthanasia in zebrafish. *ILAR J* **2012**, *53* (2), 192-204.
41. Ghobrial, G. M.; Anderson, K. D.; Dididze, M.; Martinez-Barrizonte, J.; Sunn, G. H.; Gant, K. L.; Levi, A. D., Human Neural Stem Cell Transplantation in Chronic Cervical Spinal Cord Injury: Functional Outcomes at 12 Months in a Phase II Clinical Trial. *Neurosurgery* **2017**, *64* (CN_suppl_1), 87-91.
42. Shin, J. C.; Kim, N. Y.; Chang, S. H.; Lee, J. J.; Park, H. K., Effect of Patient Education on Reducing Medication in Spinal Cord Injury Patients With Neuropathic Pain. *Ann Rehabil Med* **2017**, *41* (4), 621-630.
43. Zhu, Y.; Uezono, N.; Yasui, T.; Nakashima, K., Neural stem cell therapy aiming at better functional recovery after spinal cord injury. *Dev Dyn* **2017**.
44. Yang, X. X.; Huang, Z. Q.; Li, Z. H.; Ren, D. F.; Tang, J. G., Risk factors and the surgery affection of respiratory complication and its mortality after acute traumatic cervical spinal cord injury. *Medicine (Baltimore)* **2017**, *96* (36), e7887.
45. Piazza, M.; Schuster, J., Timing of Surgery After Spinal Cord Injury. *Neurosurg Clin N Am* **2017**, *28* (1), 31-39.
46. Dray, C.; Rougon, G.; Debarbieux, F., Quantitative analysis by in vivo imaging of the dynamics of vascular and axonal networks in injured mouse spinal cord. *P Natl Acad Sci USA* **2009**, *106* (23), 9459-9464.
47. Tamayo-Orrego, L.; Torres-Fernández, O., Protocol for the combination of neurohistological techniques on vibratome obtained sections. *Biomédica* **2011**, *31* (3), 444-450.
48. Hama, H.; Kurokawa, H.; Kawano, H.; Ando, R.; Shimogori, T.; Noda, H.; Fukami, K.; Sakaue-Sawano, A.; Miyawaki, A., Scale: a chemical approach for fluorescence imaging and reconstruction of transparent mouse brain. *Nat Neurosci* **2011**, *14* (11), 1481-8.
49. Bhalala, O. G.; Pan, L.; North, H.; McGuire, T.; Kessler, J. A., Generation of Mouse Spinal Cord Injury. *Bio Protoc* **2013**, *3* (17).
50. Bo, E.; Chen, S.; Cui, D.; Chen, S.; Yu, X.; Luo, Y.; Liu, L., Single-camera full-range high-resolution spectral domain optical coherence tomography. *Appl Opt* **2017**, *56* (3), 470-475.
51. Gotzinger, E.; Pircher, M.; Leitgeb, R.; Hitzenberger, C., High speed full range complex spectral domain optical coherence tomography. *Opt Express* **2005**, *13* (2), 583-94.